



LAWRENCE  
LIVERMORE  
NATIONAL  
LABORATORY

# Deep Penetration in Aerospace Composite Materials Using Near-Infrared Laser Radiation

S. S. Wu, C. D. Boley, J. N. Florando, M. M.  
LeBlanc, W. H. Lowdermilk, S. M. Rubenchik, J.  
R. Stanley

December 14, 2012

## **Disclaimer**

---

This document was prepared as an account of work sponsored by an agency of the United States government. Neither the United States government nor Lawrence Livermore National Security, LLC, nor any of their employees makes any warranty, expressed or implied, or assumes any legal liability or responsibility for the accuracy, completeness, or usefulness of any information, apparatus, product, or process disclosed, or represents that its use would not infringe privately owned rights. Reference herein to any specific commercial product, process, or service by trade name, trademark, manufacturer, or otherwise does not necessarily constitute or imply its endorsement, recommendation, or favoring by the United States government or Lawrence Livermore National Security, LLC. The views and opinions of authors expressed herein do not necessarily state or reflect those of the United States government or Lawrence Livermore National Security, LLC, and shall not be used for advertising or product endorsement purposes.

This work performed under the auspices of the U.S. Department of Energy by Lawrence Livermore National Laboratory under Contract DE-AC52-07NA27344.

## FINAL REPORT

LABORATORY DIRECTED RESEARCH AND DEVELOPMENT 2012 FEASIBILITY STUDY  
12-FS-014

# *DEEP PENETRATION IN AEROSPACE COMPOSITE MATERIALS USING NEAR-INFRARED LASER RADIATION*

**S. WU – PI, C. BOLEY, J. FLORANDO, M. LEBLANC, H. LOWDERMILK,  
A. RUBENCHIK, J. STANLEY**

**LAWRENCE LIVERMORE NATIONAL LABORATORY**

November 30, 2012

## **ABSTRACT**

Previous work on lethality against composite material targets considered only surface deposition of laser energy, with lethality achieved via target penetration or material removal by ply separation, delamination, and blow-off in high-speed airflow. To produce lethal effect in a militarily relevant timescale, typically on the order of seconds, requires laser irradiance in the range of ten to a few hundred kilowatts per cm<sup>2</sup>. This Feasibility Study discovers that volume heating, either by direct in-depth absorption of laser energy, for example in near-infrared (IR) laser irradiation of translucent fiberglass composite, or by rapid conduction of surface-deposited energy as in the case of opaque carbon composite, can induce failure under load in seconds by softening the resin matrix at irradiance less than 100 W/cm<sup>2</sup> – one to three orders of magnitude lower than the intensity required to produce lethal effect by target penetration or material removal.

## **INTRODUCTION**

During the Cold War era, the Department of Defense (DoD) directed energy community concentrated on defeat of strategic ballistic missiles using the mid-IR, continuous wave (CW) CO<sub>2</sub> and DF lasers, with wavelengths of 10.6 and 3.8 μm respectively. Lethality was almost universally defined as target penetration and total failure of the system, and experiments concentrated on high irradiances of a few tens to a few hundred kilowatts per cm<sup>2</sup> that were required to produce lethal effect in militarily relevant timescales of a few to a few tens of seconds. Recent DoD interest has shifted to tactical threats, such as cruise missiles and unmanned aerial vehicles (UAVs), which can be countered with lower laser irradiance. Engineering developments are making available high-power lasers in the near-IR spectral region, and very recently, some data on burn-through of UAV-wing composite materials by 1-μm fiber lasers have begun to appear [Walters 2012].

However, major emphasis has remained on rapid material removal rather than thermal response and weakening of composite structures by more subtle material strength degradation mechanisms, although some work has been reported [Stonesifer 1989, Laughlin 1997]. The existing laser - composite material interaction database consists largely of measurements of ablation energy  $Q^*$  (in kJ/g) and  $W$  (in kJ/cm<sup>3</sup>) for 10.6 and 3.8- $\mu\text{m}$  laser radiation on freestanding coupon samples, often subject to airflow. At these wavelengths, organic resins used for composite materials are strongly absorbing, leading to high surface temperatures under laser irradiation that causes resin pyrolysis and formation of carbon rich char, which thermally insulates underlying material and protects it from further damage. Carbon, in its graphitic form, has a very high heat of ablation and a sublimation temperature of about 3550°C. On a per-mass basis, few materials are more thermally robust than carbon, and consequently organic resin materials have large ablation energies, making composite targets energetically costly to defeat.

Organic resins are strong absorbers in the 3–8  $\mu\text{m}$  (3300–1250  $\text{cm}^{-1}$ ) mid-IR range, but typically quite translucent in the visible and near-IR, as frequencies in this range are below electronic transitions but above the O-H, C-H and N-H stretching modes of polymer matrix materials, as indicated by Figure 1, thus allowing penetration of laser light many fiber diameters into the material. The fibers themselves can also be strongly absorbing (carbon) or transparent (glass) in the visible and near-IR spectral range. The proposition of this Feasibility Study is that weakly absorbed, more deeply penetrating near-IR radiation will soften the resin matrix resulting in structural failure under load at lower laser intensity than what is required for mid-IR lasers.

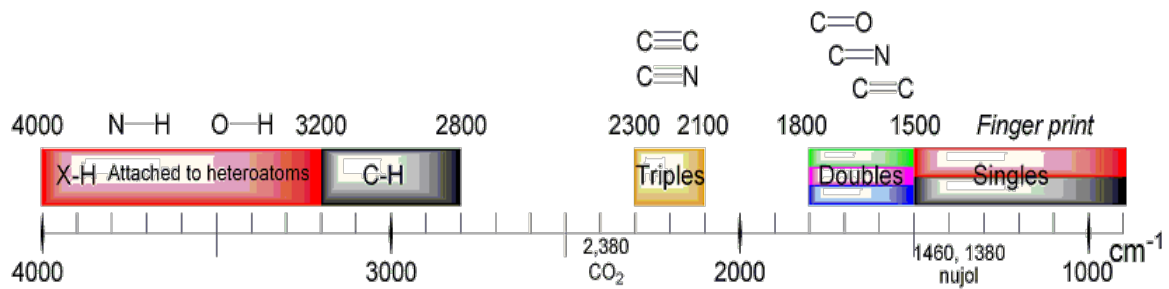


**Figure 1. Organic materials do not strongly absorb radiation with wavelength near 1  $\mu\text{m}$ , as photon energies are too low to excite electronic transitions, yet too high to excite vibrational resonances.**

Missiles that fly at speeds where aerodynamic heating is significant require a thermally robust radome with a low dielectric constant that is insensitive to temperature to ensure low bore sight error. The maximum continuous operating temperature for a typical S-glass reinforced epoxy composite is about 180°C, although these materials may be used at higher temperatures for short times. Missile radomes, for example, are single use by design, so higher temperatures may not be an issue, as the missiles have to operate for only a few minutes. Use of silica (quartz) fiber rather than glass increases the continuous operating temperature above 200°C and operating temperatures of 400°C can be achieved using polyimide or polybenzimidazole resins [Lubin 1969].

Carbon fiber is black and conducts electricity to varying degrees, and thus is not used for missile radomes or circuit boards, but is used where low weight and high strength and modulus are

required, such as in aerospace structural materials. The fibers also have high thermal conductivity and can withstand very high temperatures without significant loss of strength.

## EXPERIMENT PLAN

The purpose of this Feasibility Study was to determine whether near-IR laser radiation could penetrate more deeply into structural composite materials and have, as a result, enhanced lethality effect against composite material targets of military interest such as missile radomes, solid rocket motor casings, and UAVs. The experimental plan was to determine absorption properties, both by experimental measurement and model analysis, in samples of carbon fiber and fiberglass composite materials representative of those used for these applications and subsequently measure the compressive load strength under near-IR laser irradiation. The laser used for these experiments was a semiconductor diode laser array emitting at approximately 0.8  $\mu\text{m}$  acting as surrogate for a high-power diode-pumped alkali laser (DPAL) of the type currently under development by LLNL for directed-energy defense applications. To enable possible future detailed modeling and simulation of laser interaction with composite material targets, digital image correlation (DIC) techniques, in which the sample is photographed by synchronized, high-speed, stereo image cameras, were used to record details of sample deformation under load. Failure events were recorded also by conventional video camera and by thermal imaging camera, previously calibrated by reference to thermocouple measurements to allow standoff measurement of sample temperature.

The experimental plan consisted of the following tasks

- Acquire samples of representative carbon fiber and fiberglass composite materials. The materials tested in this study were: IM7 carbon fiber with K3B resin, a widely used aircraft structural composite material, supplied internally by LLNL, and Hexcel S-glass S-2 fiber with F155 resin supplied by the Naval Surface Warfare Center – Crane, as a representative missile radome material.
- Fabricate samples for mounting in a hydraulic load machine
- Design, fabricate and install grips for compression loading
- Design, build, and install mounting hardware for 500 and 1500 watt diode laser arrays to illuminate test samples on the hydraulic load machine in Building 231
- Calibrate the thermal image camera using thermocouple measurements of laser-heated samples
- Establish digital image correlation measurements in conjunction with the hydraulic test machine and diode laser array operations
- Measure baseline engineering stress versus engineering strain to failure at room temperature
- Conduct experimental measurements using the compact, high-power diode laser array to simulate target irradiation by the DPAL on composite samples to characterize failure under compressive load
- Conduct post-test examination and analysis of samples

- Build a ray-trace model for laser interaction with fiber composite material and use to calculate absorption, scattering, intensity distribution within the sample and field enhancement

## PRE-TEST MODELING

Composite materials consist of fibers embedded in a resin matrix where, in contrast to metals, light can penetrate significantly into the material because the absorption length is determined by the particular fiber configuration and composition of the fiber and resin materials. Furthermore, since the scattering length is typically shorter than the absorption length for the laser light, multiple scatterings occur before absorption. Direct measurement of absorptivity in composites is difficult and depends on the material structure, as shown in the experimental section. A ray-trace model was developed that determines material absorptivity from first principles in terms of refractive indices of the components and their geometry, as well as absorption depth and other important quantities such as enhancement of optical power within the material due to internal scattering. A macroscopic model also was developed that provides insight and overall results.

An optical model of composite material consists of parallel fibers embedded in the resin matrix. Macroscopic quantities of interest were determined by calculating successive Fresnel reflections and refractions within the material. While greatest interest is the 0.8- $\mu\text{m}$  wavelength of the DPAL, wavelengths in the 0.5–4  $\mu\text{m}$  range, which includes YAG, frequency-doubled YAG, COIL, HF, and DF lasers, were investigated for one composite. Specular and Lambertian components of scattered light, which can be observed experimentally, were calculated. Evidence of locally enhanced optical energy density within the material was found.

Both carbon and fused silica composite materials were modeled. These have quite different optical properties and correspondingly different laser interactions. Generalization of the model to more complex fiber geometry, even to nanoparticles, is straightforward. Light propagation in a composite material is a special case of radiation transport in turbid media. For most situations, a simplified “two-flux” macroscopic model provides a good description of experiments. This model includes parameters that must be determined experimentally. Such measurements are more difficult than might be supposed, and the interpretation of the data is not straightforward; however, parameters of macroscopic models can be derived from the microscopic description, and the phenomenological model verified.

## OPTICAL MODEL

Typically, the volume fraction of fibers in composite materials is 40–60%, with a typical fiber diameter of 10–30 microns and ply thickness of several hundred microns. Only a single ply was modeled, within which all fibers have the same orientation. A neighboring ply may have a different orientation, and the model can be generalized to multiple plies with different fiber orientations or weave patterns.

Figure 2 shows a schematic cross section of a ply with multiple rows of fibers running parallel to the surface and an incident laser beam. The fibers, seen in cross section, were modeled as identical cylinders with nominal radius  $a = 5 \mu\text{m}$ , initially arranged in regular rows and spaced to

give 50% volume fraction. The rows were then translated parallel to one another by random amounts, and finally positions of the individual fibers were randomly perturbed. Each run involved a new set of randomizations. Results were found not to be very sensitive to positions of the fibers and varied somewhat with the volume fraction of fiber and epoxy, with 50% chosen as a nominal value for purpose of initial estimates. To simulate a large spatial extent parallel to the surface, fictitious mirrors were placed within the epoxy near the edges of the incoming beam as indicated in Figure 2.

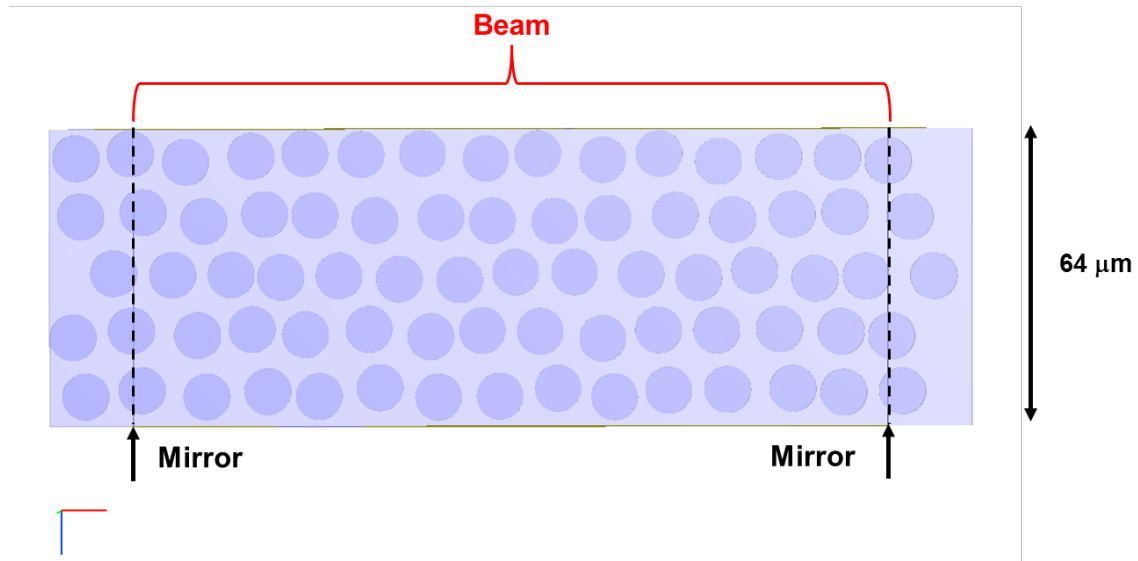


**Figure 2. Schematic geometry of the carbon-fiber model. The fibers, seen head-on, are first arranged in uniform rows and then slightly perturbed. The two mirrors account for the limited extent of the beam. The fibers, or portions of them, outside the mirrors are not included in the ray-trace calculation.**

Since the fiber diameter is much larger than the wavelength of light, the laser-composite interaction could be modeled by ray-tracing [FRED]. Rays are normally incident upon the surface, with the electric field either parallel to the fibers (“s-polarized”) or perpendicular (“p-polarized”). Because of the assumed planar geometry, the polarization remains s or p throughout multiple scatterings.

When the incoming beam encounters the surface of the epoxy, a fraction of the power is Fresnel-reflected. The real part of the epoxy index of refraction is taken to be  $n_{e,r} = 1.6$ , independent of wavelength. This can differ by a few percent from material to material. Neglecting for the moment the imaginary part, which is a few orders of magnitude smaller, the surface reflectivity of the epoxy is:

$$R_0 = \left( \frac{1 - n_{e,r}}{1 + n_{e,r}} \right)^2 \approx 0.053 \quad (1)$$

After passing through the surface, the beam undergoes multiple scattering interactions with the fibers, which are qualitatively different for carbon and fused silica fibers and are discussed separately below.

### CARBON FIBER COMPOSITE: SCATTERING

Carbon is quite absorptive at optical and near-infrared wavelengths as indicated by the substantial imaginary part of the refractive index [Borghesi 1981] plotted versus wavelength in Figure 3. At  $0.8 \mu\text{m}$ , for example, the interpolated value of refractive index is  $n_c = 3.08 + 1.88i$ .

Irregularities in the data near  $0.6$  and  $1.1 \mu\text{m}$  may be due to the differing systematics of juxtaposed experiments.

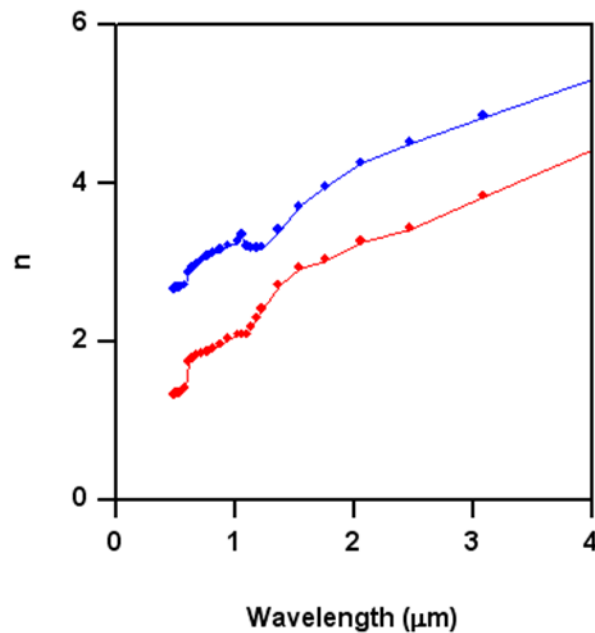


Figure 3. Index of refraction of carbon (graphite, ordinary mode) versus wavelengths, from data given in [FRED]. Upper blue line: real part; lower red line: imaginary part.

Figure 4 shows absorptivity as a function of angle of incidence for  $0.8\text{-}\mu\text{m}$  radiation in epoxy, incident on carbon as calculated from the Fresnel formulas with a complex index. At normal incidence, the absorptivity is  $0.78$ , while at  $45^\circ$  it is  $0.65$  (s) or  $0.88$  (p). Also shown in this figure are absorptivities versus wavelength at an angle of  $45^\circ$ . These gradually decrease, with p polarization about  $0.2$  greater than s.

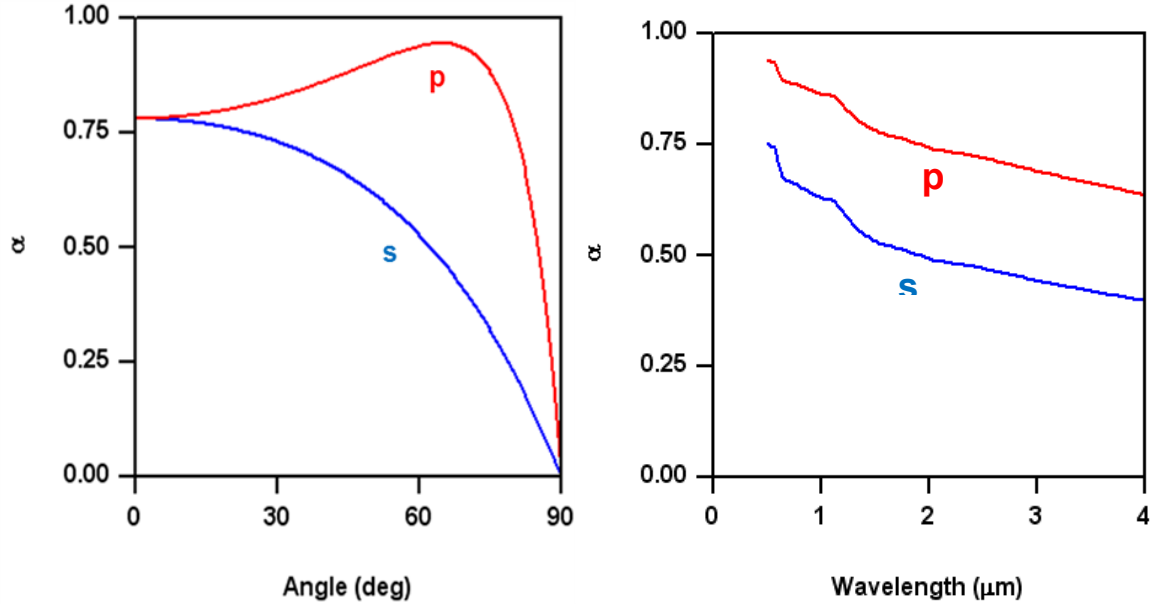


Figure 4. Fresnel absorptivity of 0.8- $\mu\text{m}$  light incident on carbon from epoxy. Left: angular dependence at 0.8  $\mu\text{m}$ . Right: wavelength dependence at 45°.

When a ray encounters a carbon fiber, the power transmitted into the fiber is assumed to be completely absorbed, since the absorption length in carbon,  $l_a = \lambda / (2\pi \text{Im} n_c)$ , is much smaller than the fiber radius. At a wavelength of 0.8  $\mu\text{m}$ , for example, the absorption length is 0.07  $\mu\text{m}$ , compared with a nominal fiber radius of 5  $\mu\text{m}$ . Only the reflected ray, with an appropriately diminished power, is followed in the ray tracing.

The negative curvature of the fiber surface produces a divergence of ray trajectories. Therefore, rays become quickly randomized in direction after a few scatterings, as illustrated in Figure 5. As a result, specific positions of the fibers do not appreciably affect the results, justifying assumptions of the model. The paucity of rays near the bottom shows that almost all the power is absorbed within the first few rows of fibers. In the model, rays reaching the lowest surface are absorbed.

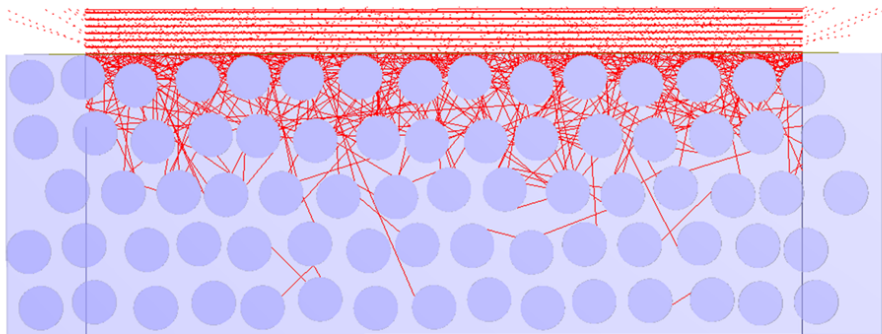


Figure 5. Sample rays within the epoxy, with carbon fibers, after several steps. In a step, each ray advances from one surface to the next. The pattern at the top indicates reflected rays.

To arrive at a reasonable number of rows to model the carbon composite, test cases with 3, 4, and 5 rows were run. For s-polarized rays, the fraction of power absorbed on the lowest surface decreased geometrically from 0.3% to 0.02%, and about an order of magnitude lower, depending on configuration, than for p-polarized. Five rows were used thereafter, guaranteeing less than 0.1% absorption at the bottom.

### CARBON FIBER COMPOSITE: OVERALL ABSORPTIVITY

The most prominent property of the composite material is its overall absorptivity, which is expected to be somewhat larger for p polarization than for s. It is also expected to fluctuate slightly from run to run because of the randomized positions of the fibers. These features are borne out by Figure 6, which shows the results for 40 configurations at a wavelength of  $0.8 \mu\text{m}$  and fill factor of 0.5. Absorptivities fluctuate around values of about 0.87 for s and 0.88 for p polarization, with a standard deviation of 0.004.

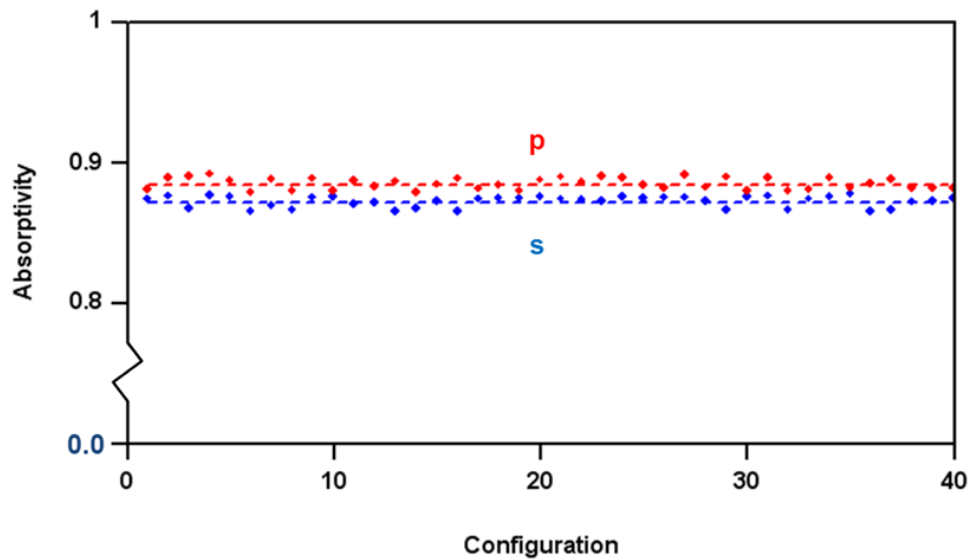
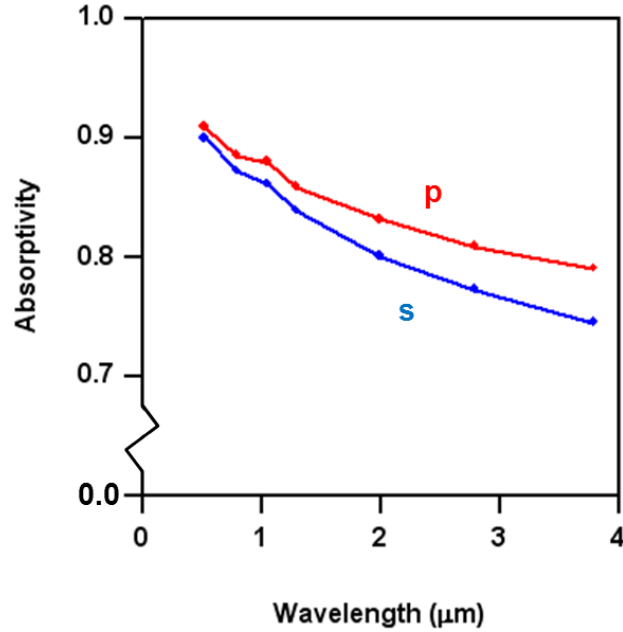


Figure 6. Calculated absorptivity of the carbon-fiber composite at a wavelength of  $0.8 \mu\text{m}$  for 40 fiber configurations. Upper points: p polarization; lower points: s polarization. The dotted lines give the averages (about 0.88 and 0.87, respectively). Each run involved  $10^6$  laser rays. Note that the vertical scale is truncated.

These values are well above the absorptivity for a single scattering from carbon, shown in Figure 4, as a consequence of the multiple scatterings. Note also that the s and p absorptivities of Figure 7 are closer to one another than for a single scattering. The reason is that an s-polarized ray tends to undergo more scatterings than a p-polarized ray. Thus, the difference in path length partially compensates for the difference in single-scattering absorptivity.



**Figure 7.** Calculated absorptivity of the carbon-fiber composite versus wavelength. Each point represents an average over 10 configurations, with  $10^6$  laser rays each. The jump near 1  $\mu\text{m}$  is caused by the apparent irregularity in the graphite index of refraction in Fig. 2.

Next, the overall absorptivity was calculated for various wavelengths. The results are tabulated in Table 1 and plotted in Figure 7. Absorptivity decreases slowly with increasing wavelength from about 0.9 to somewhat less than 0.8, with p-polarization slightly larger than s, as expected. Note that the difference between p and s absorptivity increases with wavelength.

**Table 1: Overall absorptivity of carbon-fiber composite versus wavelength.**

Wavelength ( $\mu\text{m}$ )	Absorptivity (s)	Absorptivity (p)
0.53	0.90	0.91
0.8	0.87	0.88
1.06	0.86	0.88
1.3	0.84	0.86
2.0	0.80	0.83
2.8	0.77	0.81
3.8	0.74	0.79

In the literature, the most relevant measurement appears to be the overall reflectivity of a carbon fiber phenolic at 1.3  $\mu\text{m}$  [Freeman 2000]. Near room temperature, this corresponds to an

absorptivity of 0.93, as compared with the nominal value of about 0.85 found here. Since the specific fiber/epoxy material test parameters are not known, this qualitative agreement is encouraging.

### CARBON FIBER COMPOSITE: ANGULAR DISTRIBUTIONS

The angular distribution of reflected light has a large specular peak at angles close to zero, due primarily to reflection from the epoxy, and a diffuse component due to multiple reflections from the fibers. The specular component (about 0.054 for p-polarization, 0.055 for s) was slightly higher than the surface reflectivity, because an occasional ray penetrated the surface and suffered a back-reflection from a fiber. The diffuse component, shown in Figure 8, had an approximate cosine dependence on the angle (Lambertian). Thus, the reflection into a small surface area at a large distance was roughly isotropic, resulting from directional randomization within the epoxy, as expected. Total reflectivities were consistent with the absorptivities noted above.

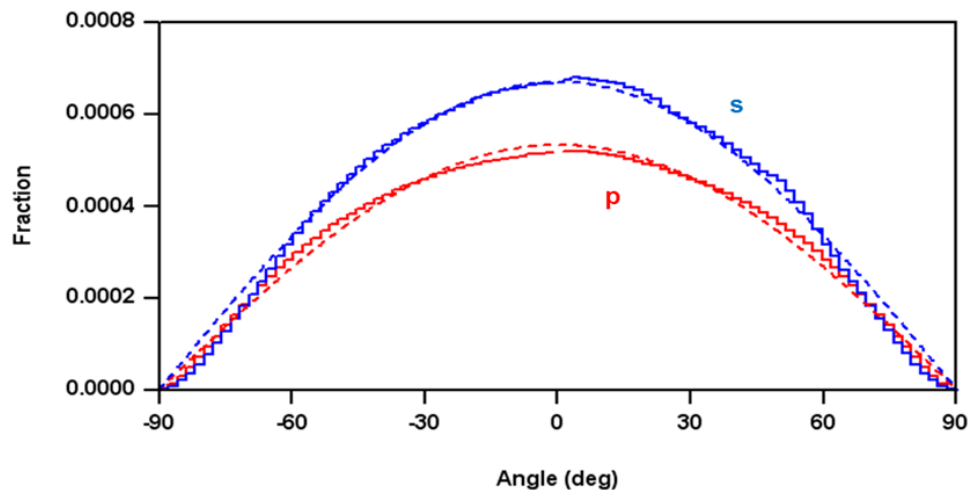
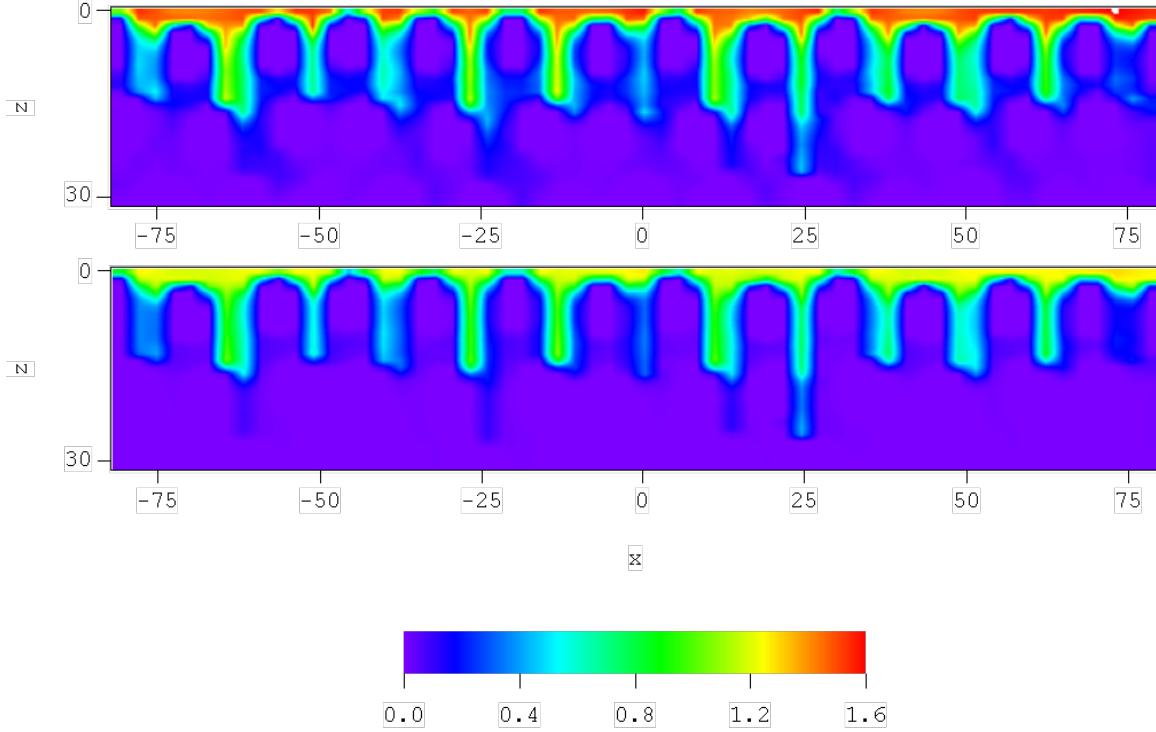


Figure 8. Calculated angular distributions of light reflected from the carbon-fiber composite, away from the specular (backwards) direction. The jagged lines show the computed results, while the dotted lines give the best fit to a function proportional to  $\cos \theta$ . The curves are normalized so that the integral gives the total diffuse reflectivity.

### CARBON FIBER COMPOSITE: FIELD ENHANCEMENT

Because of multiple reflections from the fibers, the rays in the epoxy become more densely packed in regions near the surface, shown in Figure 9. Consequently, the optical energy becomes locally enhanced with respect to that of the incident intensity, potentially leading to increased absorption in the epoxy.



**Figure 9. Local enhancement for a particular carbon fiber configuration. Top: s polarization; bottom: p polarization. Note the shadows produced by the first row of fibers.**

Within a given volume element  $V_i$  (working temporarily in 3D), the energy density associated with a particular ray  $r$  is proportional to the power of the ray and the time to traverse the element, divided by the volume of the element, i.e.,

$$u_{ir} = n_i P_{ir} l_{ir} / (c V_i) \quad (2)$$

where the index of refraction  $n_i$  accounts for the group velocity of light. On the other hand, the energy density associated with the incident flux just within the composite is:

$$u_0 = (1 - R_0) n_e P_0 / (c A_0) \quad (3)$$

Here,  $R_0$  is the surface reflectivity of Eq. (1),  $n_e$  the epoxy index of refraction, and  $A_0$  the area illuminated by the beam. The local enhancement is the ratio of the last two quantities, summed over all rays. Reverting to two dimensions, we find:

$$f_i = \frac{n_i L_0}{(1 - R_0) n_e P_0 A_i} \sum_r P_{ir} l_{ir} \quad (4)$$

where  $L_0$  is the width of the beam and  $A_i$  is the area of the element. In spite of this straightforward definition, the enhancement turns out to be surprisingly complicated to compute within the ray-trace code and was accomplished via a detailed script that runs in conjunction with the code.

Figure 10 shows the energy enhancement computed for a sample configuration, for both s and p polarization. In each case, the high-enhancement region begins at the surface and extends downward between the fibers in the first row (since the fibers are assumed to be completely absorbing, no enhancement is calculated within them). The maximum enhancement is greater for s polarization (1.6) than for p (1.3). This is as anticipated, since the former case has less absorption and therefore more scattering. With another configuration, the patterns would vary somewhat. However, one would expect nearly the same maximum enhancements.

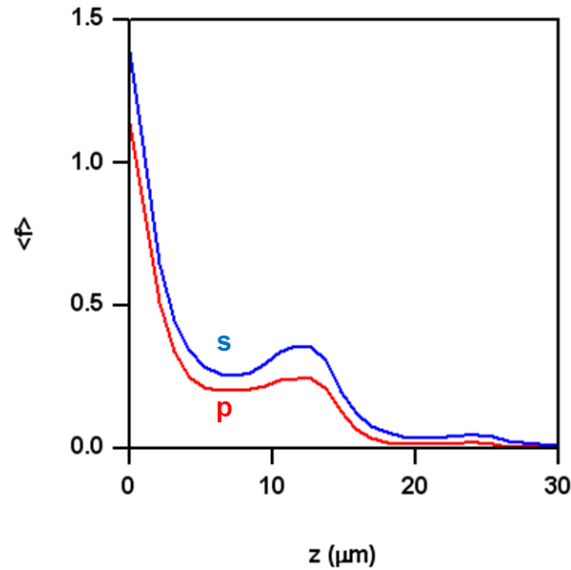


Figure 10. Average enhancement versus depth, for the distributions of the previous figure. As expected, the average is somewhat greater for s polarization than for p.

### FUSED SILICA FIBERS: SCATTERING

For our purposes, the principal difference between fused silica and carbon is that fused silica is transparent at the main wavelength of interest ( $0.8 \mu\text{m}$ ). Thus, the radiation extends much deeper into the material, limited only by absorption in the epoxy. An absorption length of 2 mm was used in the calculations below, although the results may be extended to other cases.

The index of refraction  $n_g$  of fused silica at  $0.8 \mu\text{m}$  is about 1.453 [Wolfe 1985], with negligible absorption. Since this index is smaller than that of the epoxy, a ray striking a fiber is totally reflected when its angle of incidence is greater than the critical angle for internal reflection of  $\theta_0 = 65.3^\circ$ . The Fresnel transmission coefficient from epoxy into fused silica is plotted as a function of angle in Figure 11. Roughly speaking, rays striking a fiber with angles less than about  $60^\circ$  are completely transmitted, while rays with angles greater than this are completely reflected. Also shown in this figure is the Fresnel transmission for rays incident on the fiber/epoxy surface from inside the fiber. This is nearly total for angles less than about  $60^\circ$ .

Consequently, for incident angles  $\theta$  less than about  $60^\circ$ , the path with highest power of a typical incident ray passes once through the fiber, as illustrated in the left-hand plot of Figure 11. The net scattering angle is  $2(\theta' - \theta)$ , where  $\theta'$  is the transmitted angle in fused silica

$(n_e \sin \theta = n_g \sin \theta')$ . Since the two indices of refraction are comparable, the scattering is rather slight. For example, a ray arriving at  $30^\circ$  to the normal is scattered by only  $6.8^\circ$ . This angle would increase for a larger ratio of indices  $n_e / n_g$ .

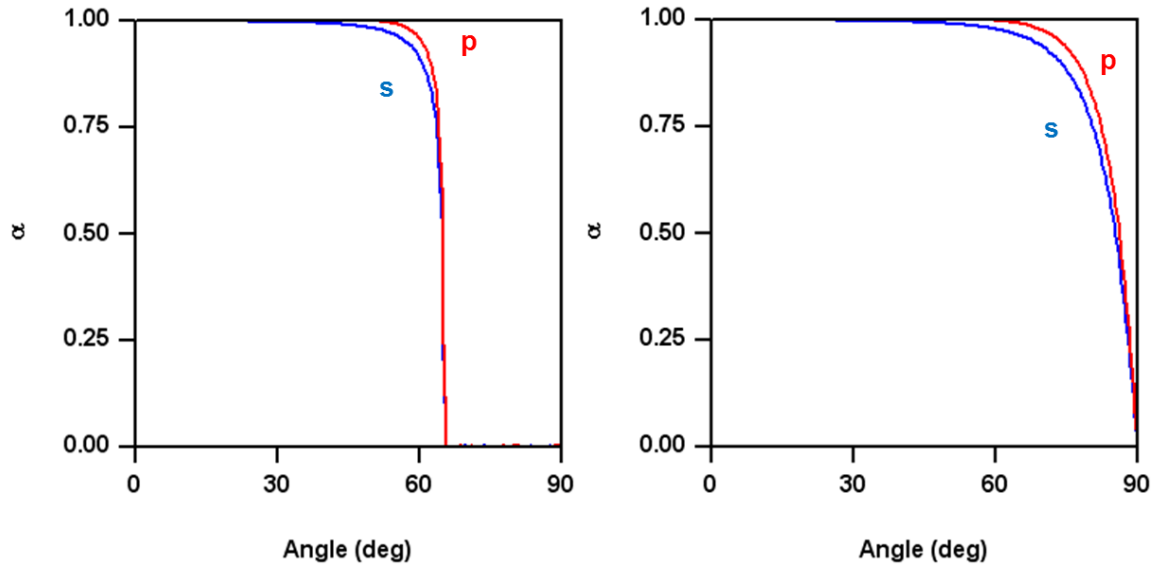


Figure 11. Left: Fresnel transmission of  $0.8\text{-}\mu\text{m}$  light incident from epoxy onto fused silica. Right: transmission for incidence from fused silica onto epoxy.

It should be pointed out that the ray-tracing code follows not only the path of greatest power but also paths with lesser power, within prescribed limits. When the power on a particular ray decreases by a factor of 105, the ray is dropped from the calculation.

As an example of multiple scattering from a single fiber, the right-hand plot of Figure 12 illustrates the scattering that would result if the ratio of fiber/background indices of refraction were considerably smaller than the case considered here. Note the multiple reflected rays.

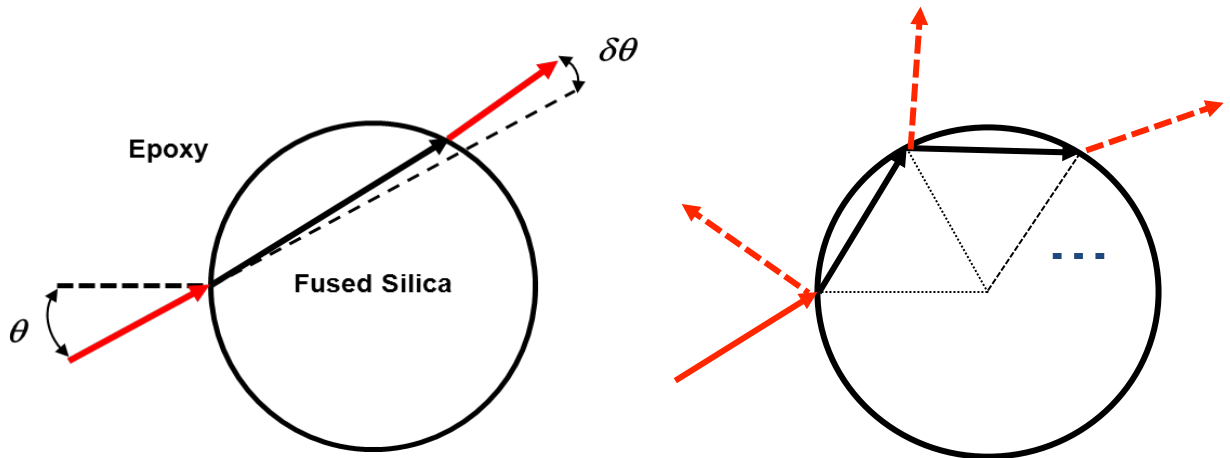


Figure 12. Left: Dominant scattering of a ray from fused silica. The incident ray arrives at  $\theta = 30^\circ$  to the normal, and the outgoing ray is diverted from this by a net angle of  $\delta\theta = 6.8^\circ$ . Right: Example of

scattering in a system with a smaller ratio of fiber/background indices of refraction. Note the multiple reflections and the sequence of interior isosceles triangles.

### FUSED SILICA FIBERS: ABSORPTION AND ENHANCEMENT

A typical geometry for the fused silica composite is shown in Figure 13. Since the light penetrates deeply into the material, 20 rows of fibers are included. The fiber radius ( $5\ \mu\text{m}$ ) and the relative fiber/epoxy areas (50/50) were the same as in the carbon-fiber case.

Figure 14 shows the local enhancement pattern calculated for this geometry and p polarization. The case with s polarization is not much different. The maximum is about 2.1. The intensification is small due to the close refractive indices of the fibers and epoxy. Of the incident power, about 12% was reflected. The fraction absorbed at the bottom was 72%. Thus, about 16% was absorbed by the epoxy.

Figure 15 shows the average enhancement (averaged parallel to the surface) versus depth. This consists of successive narrow peaks and valleys, corresponding respectively to the space between rows of fibers and the fibers themselves. The maximum value of about 1.5 is reached at about  $98\ \mu\text{m}$ , just before the ninth row.

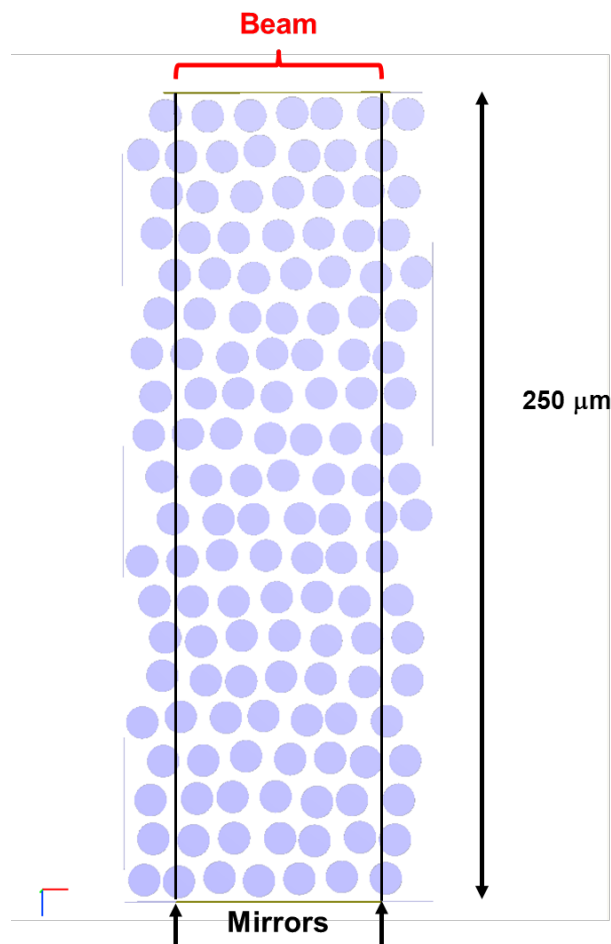


Figure 13. Typical geometry of the fused-silica composite model.

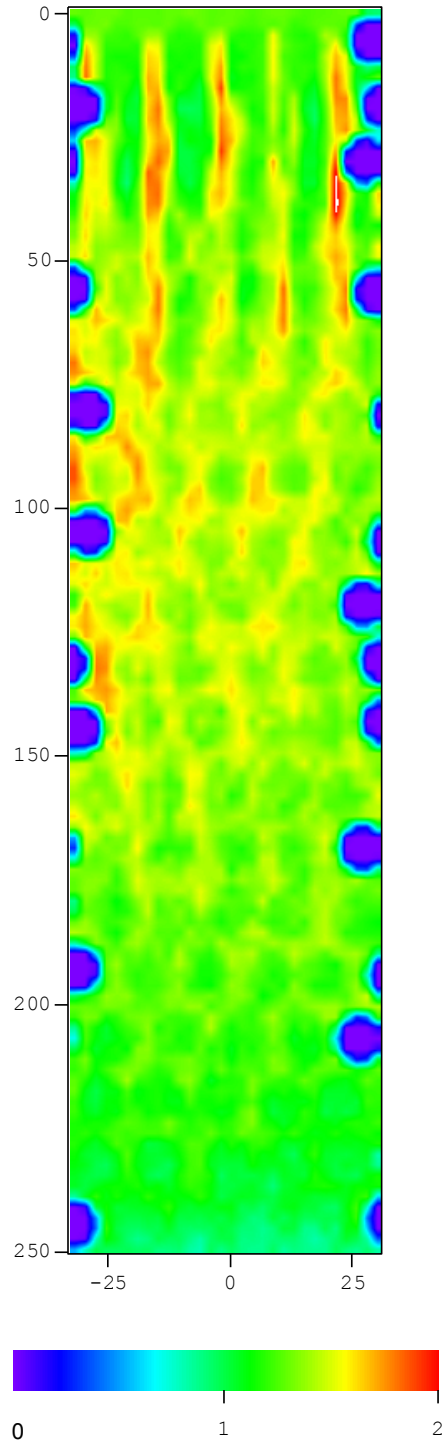


Figure 14. Local enhancement for fused silica fibers. The maximum enhancement is 2.1. The null areas (blue) along the sides indicate areas in which the enhancement was not calculated, due to complications caused by reflections.

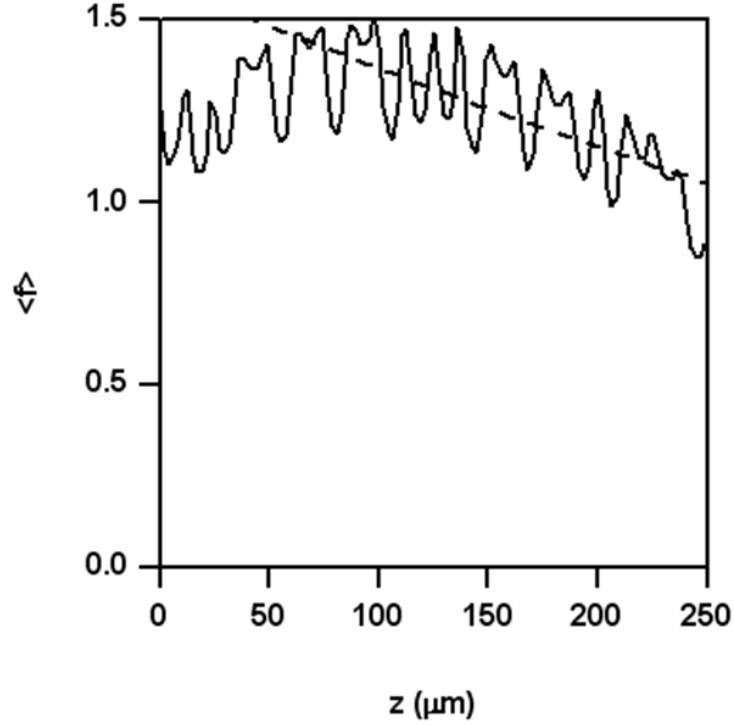


Figure 15. Average enhancement versus depth, for the distribution of the previous figure. The dashed line shows the result from the two-flux model.

### CONNECTION WITH MACROSCOPIC MODEL

The microscopic, first principles model for light propagation in a composite material described above is quite expensive computationally. Simple macroscopic models for radiation transport in scattering media also exist [Ishimaru 1978, Zeldovich 1967]. The following two-flux model, for example, is extensively employed in industry and provides a good description of experiments [Mudgett 1971].

In the two-flux model, radiation is divided into two fluxes. One flux ( $F_+$ ) propagates in the direction of the incident radiation, and the other flux ( $F_-$ ) propagates in the opposite direction. The steady-state equations describing light propagation are [Ishimaru 1978]:

$$\begin{aligned} \frac{dF_+}{dz} &= -(K + S)F_+ + SF_-, \\ \frac{dF_-}{dz} &= (K + S)F_- - SF_+. \end{aligned} \tag{5}$$

Here, the positive constants  $K$  and  $S$  describe radiation damping and scattering respectively. These equations are to be solved in a slab of thickness  $h$ . They are subject to the boundary conditions,  $F_+(0) = F_0, F_-(h) = 0$ . These conditions state that just within the slab, the positive-flowing flux equals the incident flux  $F_0$ , and at the opposite end, the backward-flowing flux vanishes.

Each of the fluxes consists of two terms, one varying as  $\exp(-pz)$  and the other as  $\exp(pz)$ , with  $p = +[K(K + 2S)]^{1/2}$ . The solution of Eq. (5) gives:

$$F_+(h) = F_0 \frac{(a^2 - 1)b}{a^2b^2 - 1}, \quad F_-(0) = F_0 \frac{a(b^2 - 1)}{a^2b^2 - 1} \quad (6)$$

where

$$a = \frac{K + 2S + p}{K + 2S - p}, \quad b = e^{ph} \quad (7)$$

Conversely, if the transmission coefficient  $T = F_+(h)/F_0$  and reflection coefficient  $R = F_-(0)/F_0$  are known, then the constants K and S are determined in the governing equations via:

$$K = \frac{(a' - 1)\ln b'}{(a' + 1)h}, \quad S = \frac{2a'\ln b'}{(a'^2 - 1)h} \quad (8)$$

where

$$\begin{aligned} a' &= (1 + R^2 - T^2 + [(1 + R^2 - T^2)^2 - 4R^2]^{1/2}) / 2R, \\ b' &= (1 - R^2 + T^2 + [(1 + R^2 - T^2)^2 - 4R^2]^{1/2}) / 2T. \end{aligned} \quad (9)$$

Averaging over  $x$  gives the desired  $z$ -dependence. By using the calculated transmission and reflection constants, one can then solve for the distribution of the light inside the sample, according to the two-flux model.

Results for the fused silica fiber case is shown in Figure 14. Here we used a transmission coefficient of 0.7 and a reflection coefficient of 0.07 (in the latter, the incident reflectivity has been subtracted). Because of problems caused by scattered light near the surface, which are common to all macroscopic models [Ishimaru 1978], an overall normalization was applied to the two-flux solution. Beyond a narrow layer near the surface, good description of the behavior of the average flux is achieved. The damping and scattering coefficients follow from Eqs. (8) and (9) as  $K^{-1} = 950 \mu\text{m}$  and  $S^{-1} = 2600 \mu\text{m}$ .

## EXPERIMENTAL DESIGN

### EXPERIMENT SETUP ARRANGEMENT

This section describes experiments to characterize laser interaction with carbon and fiberglass composite materials under compressive load using the apparatus shown in Figure 16. Samples were held vertically in a hydraulic load machine designed to apply constant compressive force. A diode array was used as a low cost surrogate light source to simulate the effects of a high-power directed energy laser on the target samples. Light from a 1.5-kW diode laser array, with

wavelength of 0.8- $\mu\text{m}$ , is passed through a lens duct and imaging lenses and provided uniform illumination on the samples. A digital video camera and IR thermal imaging camera recorded the event from the laser illuminated side. The FLIR SC-325, an IR thermal imaging camera, was used with recommended factory calibration. This camera was placed at approximately 30° from the sample surface normal and provided the capability to monitor temperature of the samples remotely. A SONY HDR-CX260V 1920x1080, full HD 60p video camera recorded real time images of the sample under test. A digital image correlation (DIC) system directly behind the sample recorded full-field, in-plane and out-of-plane displacements at several frames per second. An exhaust trunk mounted above and behind the sample removed fumes released by the laser heating process.

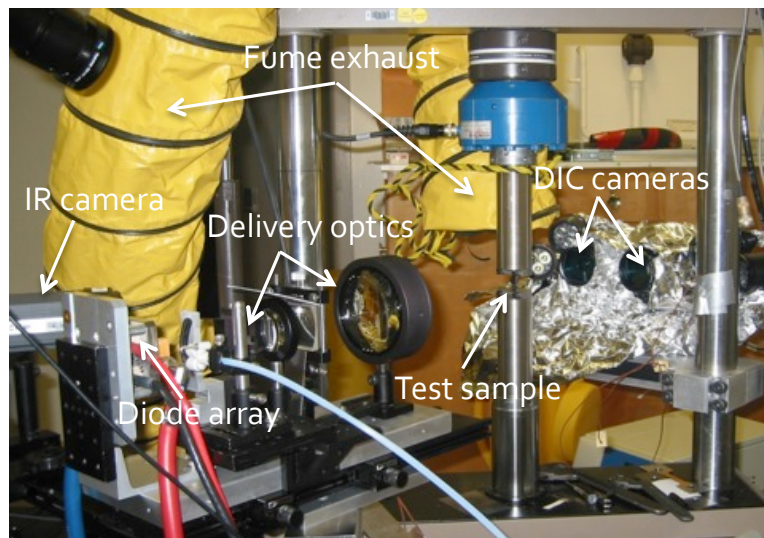


Figure 16. Experimental setup for compression tests on composite samples.

### DIODE ARRAY AND BEAM DELIVERY OPTICS

A commercial 20-bar diode laser array was used, producing 1.5-kW of 780-nm light at a maximum current level of 87-A. The FWHM linewidth of the radiation varied from 2 nm at low power to 4 nm at maximum power. To produce a uniform beam profile on the sample, light from the diode array was passed through a lens duct several inches in length before being imaged by a 100-mm lens onto the samples. Radiation intensity on the samples was determined by measuring the transmission through a small 1 x 3 cm rectangular aperture at the image plane. The beam was relatively uniform across the aperture area, allowing reasonably accurate measurement of radiation intensity. Flux was measured with a Coherent PM300F-50, 300-W max fan-cooled thermopile with broadband coating and 50-mm aperture. A false color image of the laser radiation at the sample plane is shown in Figure 17. This image was taken with a Point Grey Chameleon monochrome 1.3-MP imaging CCD camera with 12-bit A/D converter.

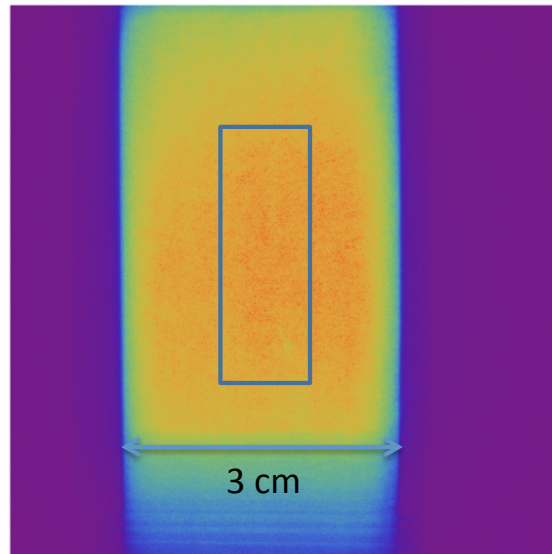


Figure 17. Diode array radiation pattern after lens duct and  $f = 100$  mm imaging lens. The rectangular box denotes the approximate location of the 1 x 3 compression test samples in the beam. This image was taken at a diode current level of 25 A.

### HYDRAULIC TEST MACHINE

The test machine used was an MTS Systems Corporation computer-controlled, servo-hydraulic 20-kip machine. The sample was loaded in displacement control to the desired load, which was maintained in load control through sample failure. The 304 stainless steel grips were designed for maximum rigidity without using a sub-press style grip.

### SAMPLE SELECTION AND PREPARATION

The carbon fiber test material chosen for the compression test was IM7/K3B, a composite made of IM7 graphite fibers in an amorphous thermoplastic polyimide resin designated K3B. The glass transition temperature ( $T_g$ ) of K3B has been reported to be  $236^\circ\text{C}$  [Feldman 1996], which allows use of IM7/K3B for elevated temperature applications, such as high-speed aircraft or missiles. The samples tested had 16 plies with fiber orientation rotated  $45^\circ$  in successive layers, thus giving four plies each at  $0^\circ$ ,  $+45^\circ$ ,  $90^\circ$ ,  $-45^\circ$ . The fiberglass test material was Hexcel Corporation's HexPly S-2 glass fabric in an 8-harness satin weave (nominal 65% volume fraction of fiber) with F155 resin, a thermoset epoxy with  $T_g$  of  $120^\circ\text{C}$ . Hexcel designation for this material is "1581-38-155". Test samples were provided by Naval Surface Warfare Center – Crane, as representative of missile radome material. Three samples of each material with dimensions 1 x 5 cm were prepared. Thicknesses of the carbon and fiberglass samples were 2.2 mm and 3.4 mm, respectively.

### STRAIN DEFORMATION MEASUREMENT

Accurate, quantitative measurement of strain deformation is required to characterize material properties and to verify material models and results of finite element simulations. Currently, such measurements are made typically by digital image correlation, a non-contact optical method for strain measurement, replacing traditional extensometer techniques that measure strain between two points, thus providing only an average strain over an area. The DIC system records full-field

strain displacement during a load test using a pair of high-speed, synchronized stereo-image cameras, and determines the strain deformation field with spatial and temporal resolution by processing the stereo images. The data processing software used here was ARAMIS, a commercial package for optical image photogrammetry. This software renders the series of stereo images into three-dimensional displacement vectors and strain vectors as functions of time, providing the 3-D displacements and velocities, surface strain values and strain rates. For ARAMIS to track deformation, the target needs a painted surface with a high contrast pattern; here, a random speckle pattern was sprayed on the surface, first with white spray paint and then with black spray paint. DIC tracks the position of the same physical points shown in a reference image and deformed image.

### **DIRECT ABSORPTION MEASUREMENT**

To measure the absorptivity of the composite materials, a set-up similar to that used for metal absorptivity measurements [LLNL 12-ERD-050] was used and is shown in Figure 18. The uniform beam produced by the diode array irradiated the sample with attached thermocouples (TC). Absorptivity was determined from the thermal balance equation:

$$w\rho(T)c_p(T)\frac{\partial T}{\partial t} = A(T)I - Q(T) \quad (10)$$

where  $w$  is the sample thickness,  $\rho(T)$  the temperature-dependent density,  $c_p$  the specific heat,  $I(t)$  the incident intensity, and  $Q(T)$  the thermal loss. Assuming thermal loss is a function only of sample temperature, *i.e.*, the loss channels are identical with and without laser illumination,  $Q(T)$  measured during cooling when the laser is off applies also during heating, then absorptivity of the sample can be determined with no ambiguity. The method assumes that the temperature is uniform across the entire sample, which was later found to be not the case for composite materials.

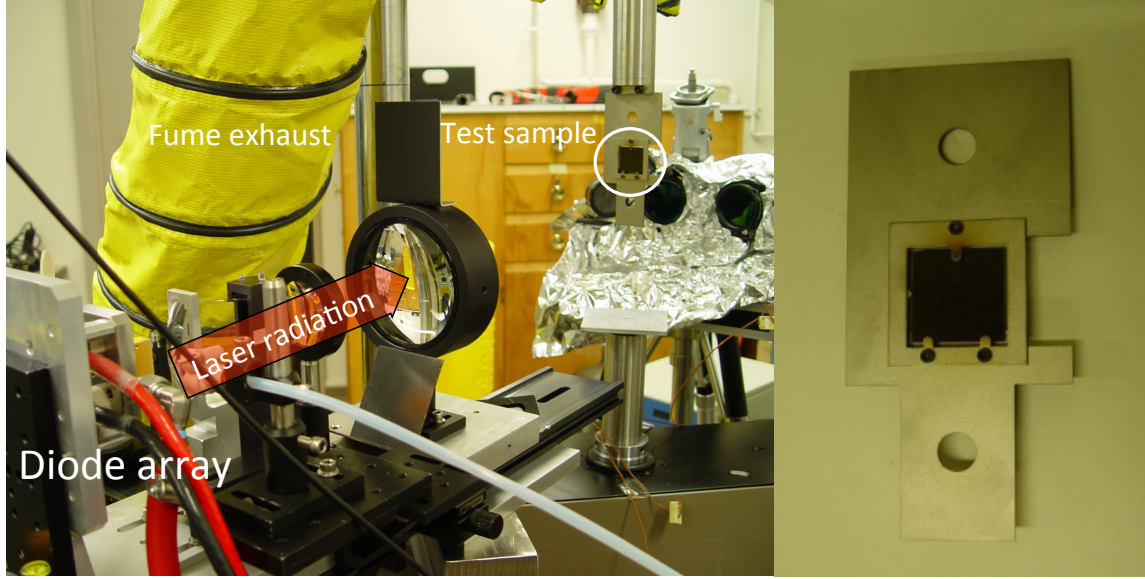


**Figure 18. Left: experiment set-up used for direct measurement of sample absorption: 1.5-kW diode array and light duct used to illuminate sample. Right: a sample held in stainless-steel mount ready to be attached with thermocouples to measure sample temperature under laser irradiation. To minimize thermal conduction, the mount holds the sample at three major points of contact.**

For carbon fiber composites, laser energy is expected to be absorbed almost entirely on the surface. Composite materials tend to have very low thermal conductivity [Chen 1995, TPRL Inc. 1999]. Thus, a thin carbon fiber sample with thickness  $w = 0.5$  mm was specially used for this measurement to minimize temperature gradients. The material consisted of layers of M55J high-modulus carbon fibers embedded in resin rotating by  $60^\circ$  from layer to layer. Using for the thermal diffusivity the value  $D = 0.003$  cm<sup>2</sup>/sec, the thermal diffusion time is found to be  $\tau \sim w^2 / D \sim 0.8$  sec. To ensure the heating times were much longer, very modest levels of irradiation, with intensity less than 10 W/cm<sup>2</sup>, were used.

Assuming that the material parameters are independent of temperature, the temperature distribution in a slab of thickness  $w$  heated on the surface at  $x = w$  with thermal flux  $F$  and thermo-isolated at  $x = 0$  is given by the expression [Carslaw 1959]:

$$T(x,t) = \frac{Ft}{\rho c_p w} + \frac{Fw}{k} \left[ \frac{3x^2 - w^2}{6w^2} + \frac{2}{\pi^2} \sum_{n=1}^{\infty} \frac{(-1)^n}{n^2} \cos\left(\frac{\pi n x}{w}\right) \exp\left(-\frac{\pi^2 n^2 t}{\tau}\right) \right] \quad (11)$$

where  $\tau = w^2 / D$  and  $k$  is the thermal conductivity. In our experiment, the temperature on the rear surface  $T(0)$  was measured, while in Eq. (10), the thermal physical constants are functions of the average slab temperature,  $\langle T \rangle$ . Integrating Eq. (11) over the slab gives

$$\langle T \rangle = \frac{Ft}{\rho c_p w} \quad (12)$$

To estimate  $T(0)$ , notice that for  $t \geq \tau$ , the series in Eq. (11) rapidly tends to zero and gives

$$\frac{T(0)}{\langle T \rangle} \approx 1 - \frac{\tau}{6t} \quad (13)$$

For  $t \gg \tau$ , the difference between the thermocouple measured temperature and the averaged temperature is small, hence calorimetric measurements of absorptivity looks promising. However, as will be described in the following section, there was still significant temperature variation between the front and rear surfaces on the sample, making this technique difficult to apply in practice.

### **CALIBRATION OF IR THERMAL IMAGING CAMERA**

It is very attractive to measure the surface temperature remotely by use of an infrared camera, which can be done for an ideal blackbody or a body with frequency independent emissivity. In reality, emissivity, the ratio of thermal radiation intensity to ideal blackbody radiation, is a function of frequency and observation angle. Much of the data on emissivity were collected in the early 20<sup>th</sup> century. Also, because emissivity is very sensitive to the particular state of the surface, much of the data may not be directly applicable. In addition, the IR camera uses only a specific range of wavelengths, which makes temperature calibration more complex.

In this study, a method was developed to measure absorptivity calorimetrically, and the recorded data can then be used to calibrate the IR camera. The diode array uniformly irradiated a thin sample of test material, and temperature was measured both directly by thermal couples (TC) and recorded by the thermal camera with different heating and cooling rates.

The FLIR SC-325 camera was used with recommended factory calibration. This camera uses a 320 x 240 pixel Focal Plane Array (FPA) and uncooled microbolometer with sensitivity in the 7.5–13  $\mu\text{m}$  spectral range. For metals, with good thermal conduction, the IR camera reading is very different from the thermocouple reading, but their ratio is a function of temperature only, and as a result, the thermal camera can be recalibrated for remote temperature measurement.

The reflectivity of composite materials is low and thermal radiation is much closer to an ideal blackbody. Due to low heat conduction, however, it takes a long time for heat to conduct throughout the sample, which can affect the measurements.

### **EXPERIMENTS WITH METALS**

Samples of Al, Ti and steel 1–2 mm thick were irradiated at 10–30  $\text{W}/\text{cm}^2$ , with temperature and temperature uniformity measured by thermocouples on the rear side of the samples and by the IR camera located at  $\sim 30^\circ$  to the surface normal. As the thermal diffusion time, even for Ti at about 0.1 sec, was much smaller than the typical heating times, good uniformity was achieved.

The temperature recorded by thermocouples and IR camera for aluminum, shown in Figure 19, differ considerably. However, the ratio of the two values, shown in Figure 20, was found to be nearly identical on both heating and cooling cycles and for two different samples: one illuminated

at  $12 \text{ W/cm}^2$  and the other at  $24 \text{ W/cm}^2$ . Thus, as the ratio of temperatures measured by the IR camera and thermocouples depends only on surface temperature, the thermocouple data provides a direct way of calibrating the IR camera.

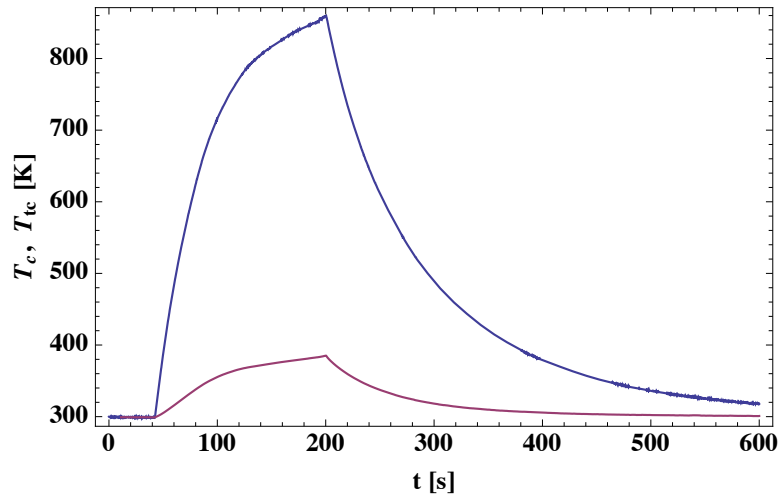


Figure 19. Temperature recorded by the FLIR camera (red) and thermocouples (blue) on an aluminum sample.

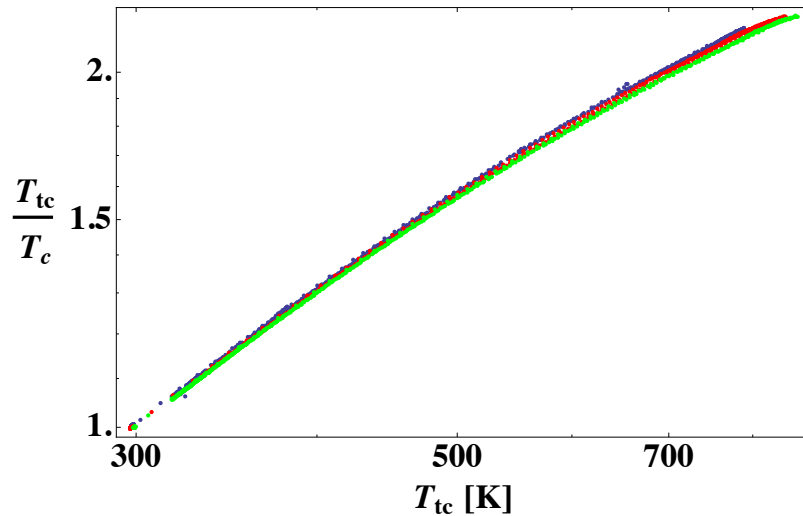


Figure 20. Ratio of temperature measured by the infrared camera ( $T_c$ ) and thermocouples ( $T_{tc}$ ) on both heating and cooling periods over three different heating cycles for an aluminum sample.

The mean free path for the photons in metals is extremely small (tens of nanometers); hence thermal radiation is determined by surface temperature. The intensity of thermal radiation from the surface  $dI$  in the element of solid angle, according to the Kirchoff's law, is related to the intensity of the blackbody radiation  $dI_0$  by the relation  $dI = A_\omega dI_0$ , where  $A_\omega$  is the absorptivity of the natural light incident on the surface [Landau 1960]. Emissivity is equal to  $A_\omega$  and varies with frequency, temperature and observation angle. As was discussed, the absorptivity of real materials, which is very different from textbook data for ideal materials, depends on surface oxide

layers, corrugation, etc., which fortunately is fairly consistent from sample to sample. The IR camera integrates thermal radiation over the wavelengths to which it is sensitive (7.5–13  $\mu\text{m}$ ), so its signal must be the function of surface temperature and observation angle only. Metal absorptivity is low for these wavelengths, and the thermal radiation is much smaller than blackbody. The absorptivity measured for Ti and Al varied little from sample to sample and depended only on the temperature, so thermocouples data could be used to calibrate the IR camera. Laser irradiation of steel produces random spots of oxide formation, which affected the thermal radiation, so reliable calibration was possible only for special situations (e.g., in vacuum) or possibly for an average over areas large compared to the oxide spots.

## EXPERIMENTS WITH COMPOSITE MATERIALS

In composite materials, the mean free path of photons is much longer than in metals, so the thermal radiation is emitted from a thicker layer of the material. If the temperature in this layer is non-uniform, the thermal radiation has information about a volume averaged “effective” temperature that is different from the actual surface temperature [Zeldovich 1967]. Also, the low thermal conductivity of composites produces high temperature gradients that can confuse the IR camera.

The first set of experiments to measure absorptivity of carbon composite used the same set up as the measurements on metals. Thin carbon composite samples ( $d \sim 0.5 \text{ mm}$ ) were specially selected to minimize temperature gradients. The thermal diffusivity of carbon composite across the fibers is  $D \sim 0.003 \text{ cm}^2/\text{sec}$  [Thermophysical Properties, 1999] with noticeable variability for different materials. The thermal diffusion time  $d^2/D$  is about 1 sec. To reduce the heating rate and ensure uniform illumination on the sample, low irradiation intensity was used. However, as discussed in the section on absorption measurements, this technique proved to be unreliable due to temperature non-uniformity.

Figure 21 shows temperatures recorded by thermocouples on the rear part of the sample and by the IR camera facing the rear side. Because absorptivity of the carbon composite is very high [Landau 1960], close to ideal blackbody radiation is expected and good correlation is observed. The ratio of  $T_{\text{TC}}$  to  $T_{\text{IR}}$  calculated from data of Figure 21 is presented in Figure 22.

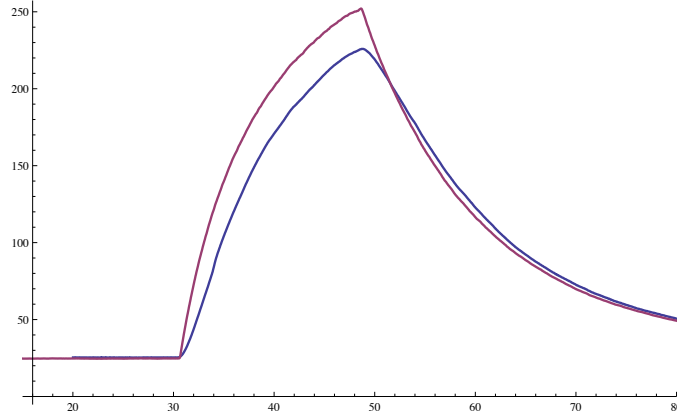


**Figure 21. Temperature readings from thermocouples attached to the rear surface of carbon composite sample versus IR camera reading from the rear surface.**

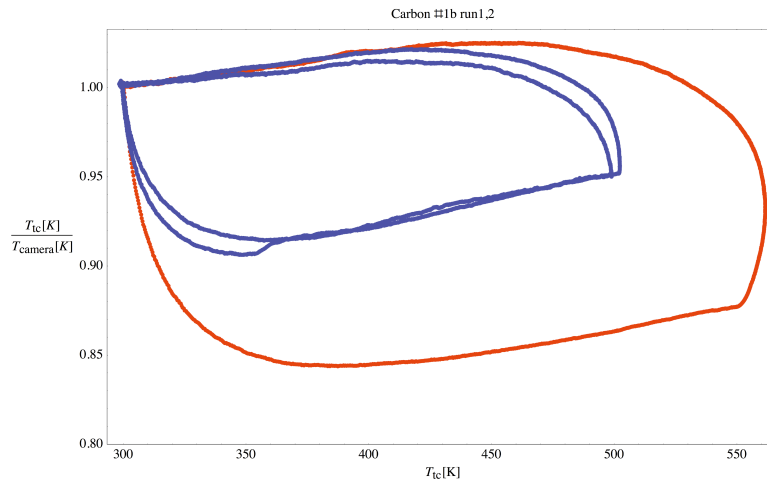


**Figure 22. The ratio of temperatures recorded by the thermocouple and IR camera from three different heating cycles on a carbon composite sample. The composite sample is illuminated at 3 W/cm<sup>2</sup> (blue) and 7 W/cm<sup>2</sup> (red). The lower portions of the curves were recorded during heating and the upper portions during cooling.**

During heating, the IR camera overestimates temperature due to thermal gradients, as the camera detects photons coming from deeper within the heated layer. Because thermal radiation is very sensitive to the temperature, even small gradients will affect the measurements. The difference in the two readings is smaller for lower pump irradiance as slower heating provides more uniform temperature. During cooling, temperature changes more slowly, allowing for temperature equilibration, and the IR camera and thermocouple results are practically identical.

The scattering length in fiberglass is much shorter than the absorption length  $l_a$ , and the light penetrates deeply into the material, with intensity decreasing exponentially on the scale  $L$ . In the two-flux approximation for radiation transport [Zeldovich 1967]:

$$\frac{1}{L^2} = \frac{1}{l_s} \left( \frac{1}{l_a} + \frac{1}{l_s} \right) \quad (14)$$

The values of absorption and scattering depth for fiberglass must be measured in a separate experiment, but our preliminary data indicates that  $L$  is of millimeter scale or larger. Hence, a much more uniform temperature distribution is expected near the front surface. Also, with expected strong absorption in the IR camera's detection range, the thermocouples and IR camera measurements may be close.

Figure 23 presents data for heating and cooling a 3.2-mm thick sample of the S-2/F155 fiberglass material as recorded by thermocouples inserted at depths of 0.8, 1.5, 2.3, and 3 mm from the rear surface (opposite the illuminated surface). The different shape for the TC closest to the illuminated surface ( $\sim 0.2$  mm) is due to more rapid cooling and possibly also due to direct light absorption by the thermocouple. Overlap of the traces for the two intermediate depth TC's is possibly due to experimental error, but could not be determined during this short study. However, the important result, shown in Figure 24, is that the ratio of temperatures recorded by the thermocouple closest to the surface ( $\sim 0.2$  mm) and the IR camera is within 5% over the entire temperature range recorded, demonstrating that the IR camera can be used for accurate remote measurement of surface temperature. The different qualitative behavior for fiberglass and carbon composite is attributed to steep thermal gradients in the carbon composite, deep light penetration in fiberglass, TC location below the surface in fiberglass and surface cooling effects.

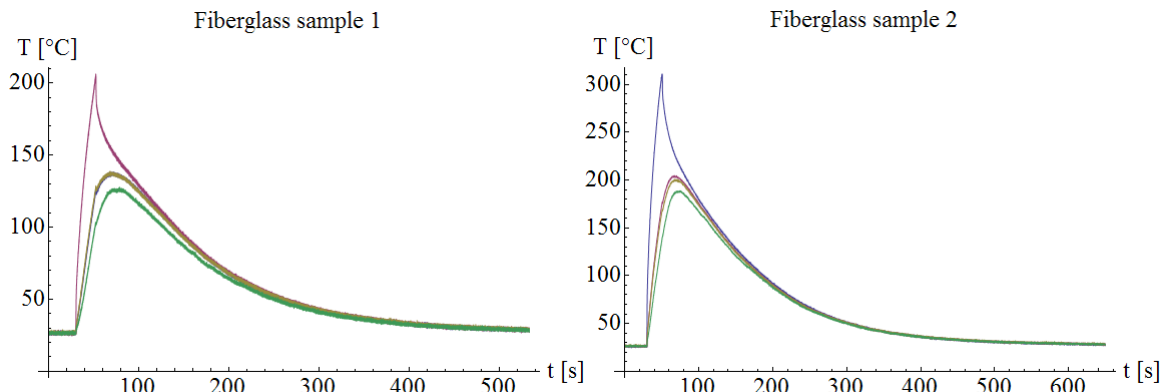


**Figure 23. Temperatures recorded by four thermocouples inserted in two 3.2-mm thick fiberglass samples at depths of 0.8, 1.5, 2.3 and 3 mm from the rear surface. The intensity on sample 1 is about  $12 \text{ W/cm}^2$ . The intensity on sample 2 is about  $21 \text{ W/cm}^2$ . The samples and thermocouples were prepared separately, and measurements were done in different experimental runs. Reason for the overlap of traces for the two intermediate depths is yet undetermined.**

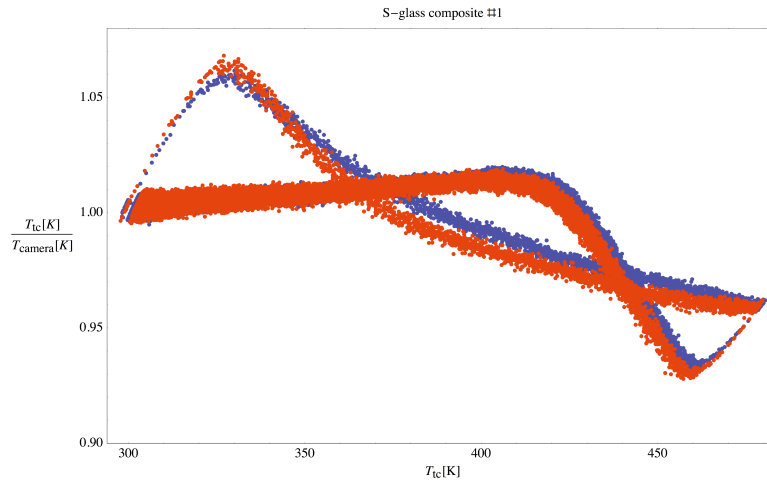


Figure 24. The ratio of thermocouple readouts and the IR camera measured temperatures of glass composite sample 1 under  $12\text{W}/\text{cm}^2$  diode laser illumination. The blue and red curves represent two consecutive heating and cooling cycles showing repeatability of measurement.

## COMPRESSION TEST RESULTS

### BASELINE COMPRESSIVE STRENGTH MEASUREMENT

A baseline, room temperature compressive strength at room temperature, in the absence of laser heating, was established by mounting test samples vertically in the hydraulic load machine and applying a slowly increasing compressive load until structural failure occurred, which typically required several minutes. In these room-temperature measurements, results shown in Figure 25, failure occurred at the grip point due to onset of classic Euler instability [Landau 1960], which defines the axial compressive load limit of unsupported columns and beams. Because the grips allow no out-of-plane displacement, when the sample starts to bow or flex under compression, stress is concentrated near the grip point causing breakage. Consequently, of course, this “baseline” room temperature failure load established by this method depends on both sample and test arrangement, not an intrinsic property of the material, and served only to define a relevant starting load for characterization of compressive failure during laser heating. The baseline failure load established by this procedure was 506 MPa for the carbon composite and 276 MPa for the fiberglass samples. Subsequent measurements of failure under laser heating were started with an initial compressive load of 50% of the room-temperature baseline failure load.

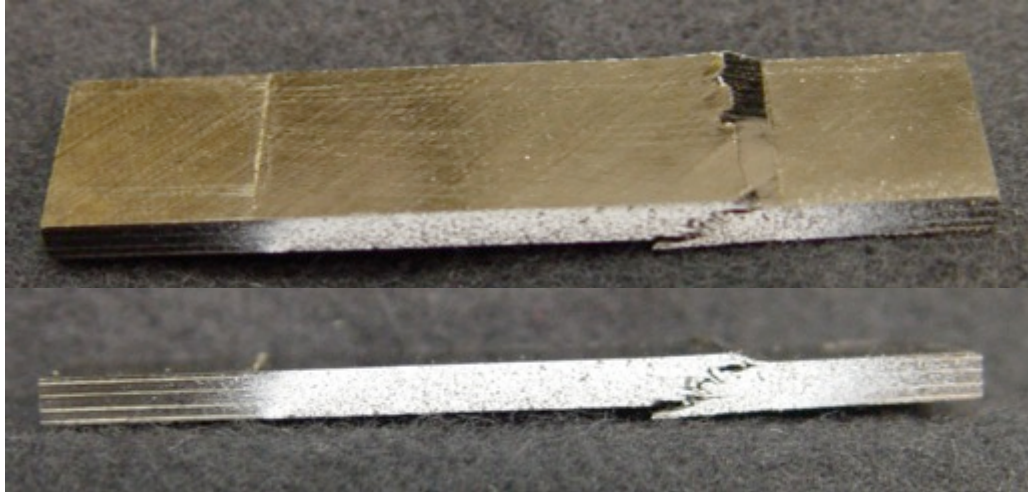


Figure 25. Carbon composite IM7/K3B sample 1 - baseline, room temperature compression strength measurement. Failure occurred at the grip point.

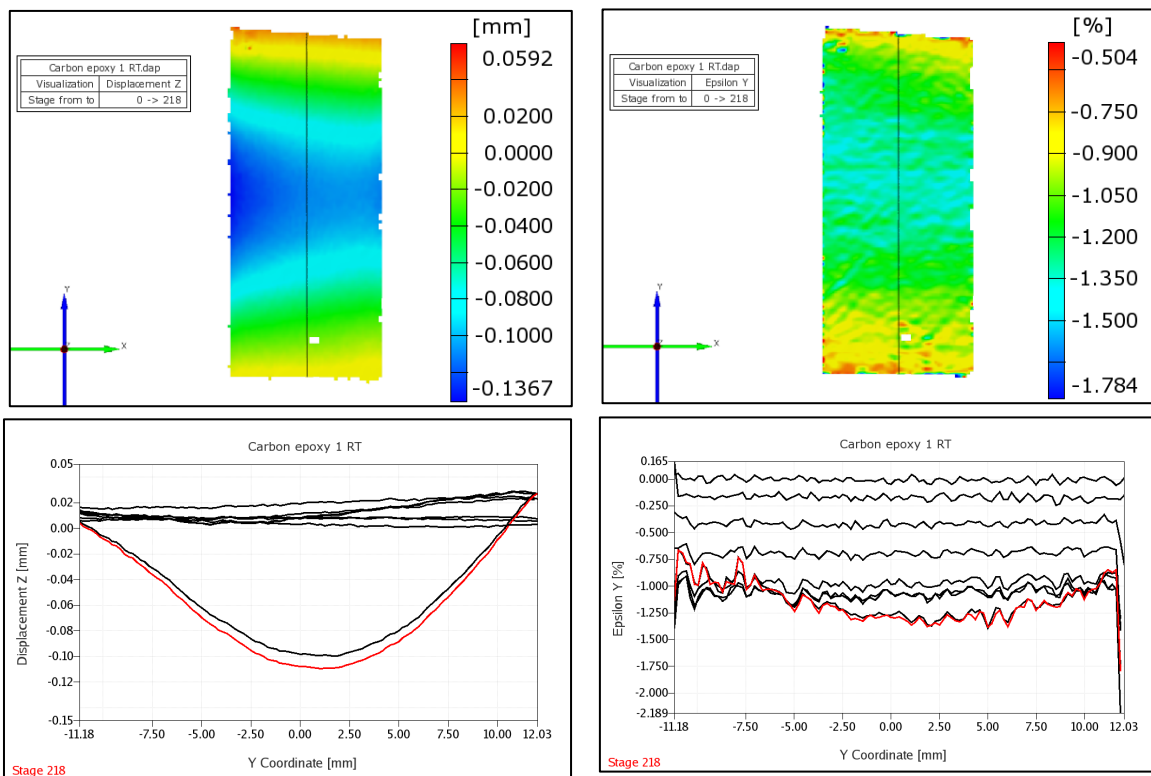


Figure 26. DIC measurements for the carbon composite sample 1 baseline compression strength. Out of plane displacement (upper left), axial strain (upper right), while lower left and right show lineouts taken along the black line in the photos above. The sample experiences 0.12  $\mu\text{m}$  out of plane displacement, away from the DIC cameras just prior to failure.

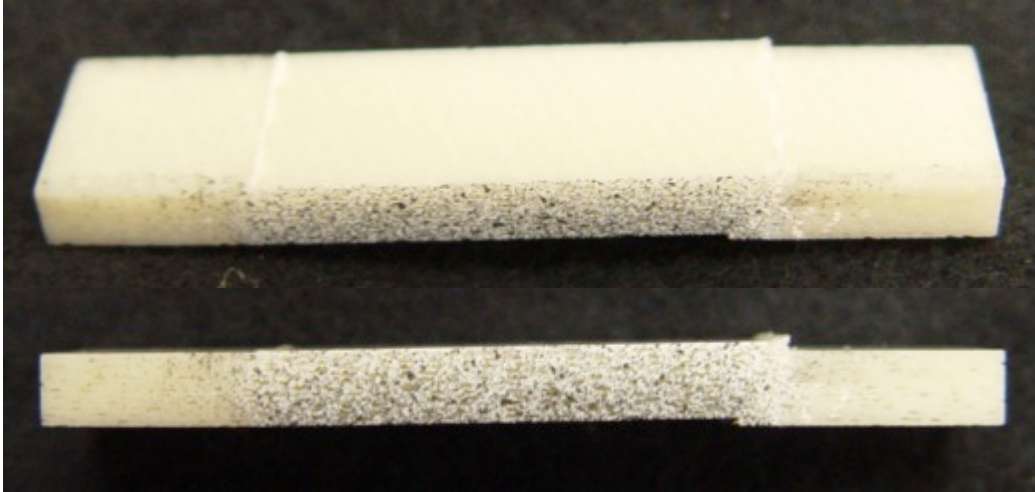


Figure 27. Fiberglass S-2/F155 sample 1, room temperature compression strength measurement. Failure occurred at grip point.

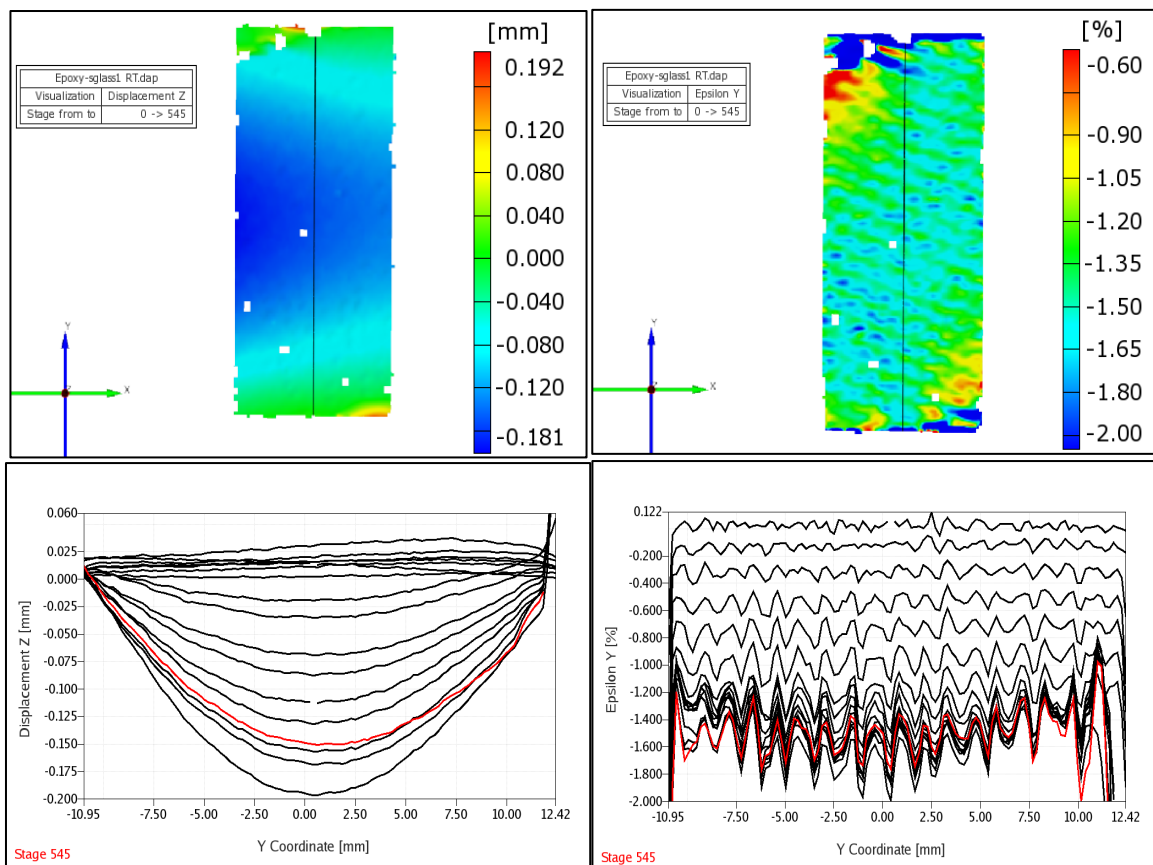


Figure 28. DIC measurements for S-2/F155 fiberglass sample 1 baseline compression strength measurement. Out of plane displacement (upper left), axial strain (upper right), with lower left and right showing lineouts taken along the black line in the photos above.

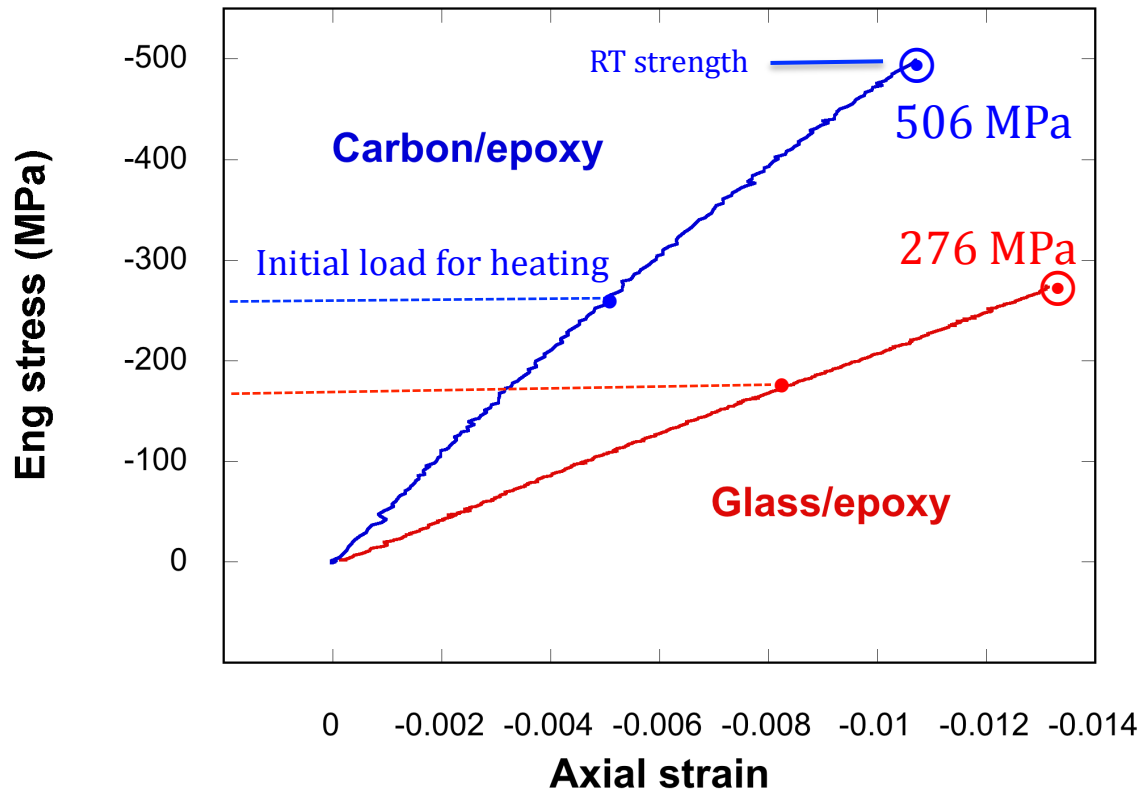


Figure 29. Engineering stress axial strain of rectangular composite samples in a compression test up to failure at room temperature.

### CARBON COMPOSITE

Using a fresh sample, the initial, 50% baseline load of 253 MPa was applied. While maintaining this applied load, the diode array illuminated the sample at specified flux until failure occurred. The initial test of a carbon composite sample was at flux of 20 W/cm<sup>2</sup>. Figure 30 shows the different steps the sample undergoes during laser irradiation. Soon after sample irradiation began, smoke appeared in (a), and then rippled features can be seen on the surface in (b). After about 4 seconds, structural failure in the form of delamination along the midsection of the sample and overall collapse began in (c), followed quickly by complete fracture of the sample in (d). The two pieces of the sample were pulled apart by the test machine on removal after cooling and are shown in Figure 31. In previous reports of laser-induced failure of carbon composite, the intensity required is typically greater than 100 W/cm<sup>2</sup> [Cozzens 2007]. Such intensity may be required for significant ablative removal of epoxy resin, but as shown here, it is sufficient to simply weaken the epoxy matrix to reduce structural integrity.

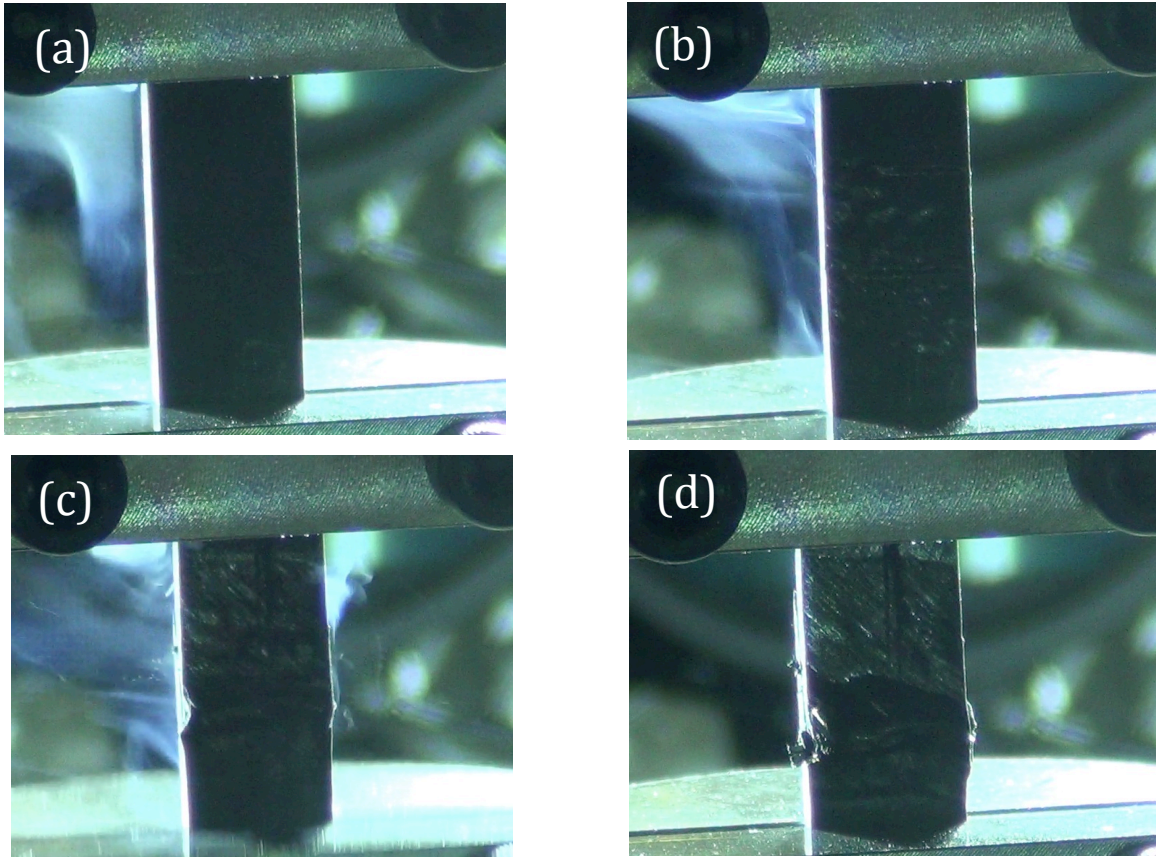


Figure 30. Carbon composite IM7/K3B sample 2, load 276 MPa, irradiated at  $20 \text{ W/cm}^2$ . Time sequence is upper left to lower right: (a) laser on, smoke appears, (b) visible surface changes, (c) compressive failure occurs at 4 s, (d) laser off – 5 s total irradiation time.



**Figure 31. Post irradiation photos of carbon composite in sample 2. Breakage resulted from the sample being forcibly pulled apart during the removal process.**

DIC measurement results, shown in Figure 32, indicate the sample had more than 0.24-mm out of plane displacement toward the cameras (away from the laser) moments before failure, consistent with the front (illuminated) surface losing structural integrity first and causing a bow toward the camera. An infrared image of the sample moments prior to failure and temperature data are shown in Figure 33.

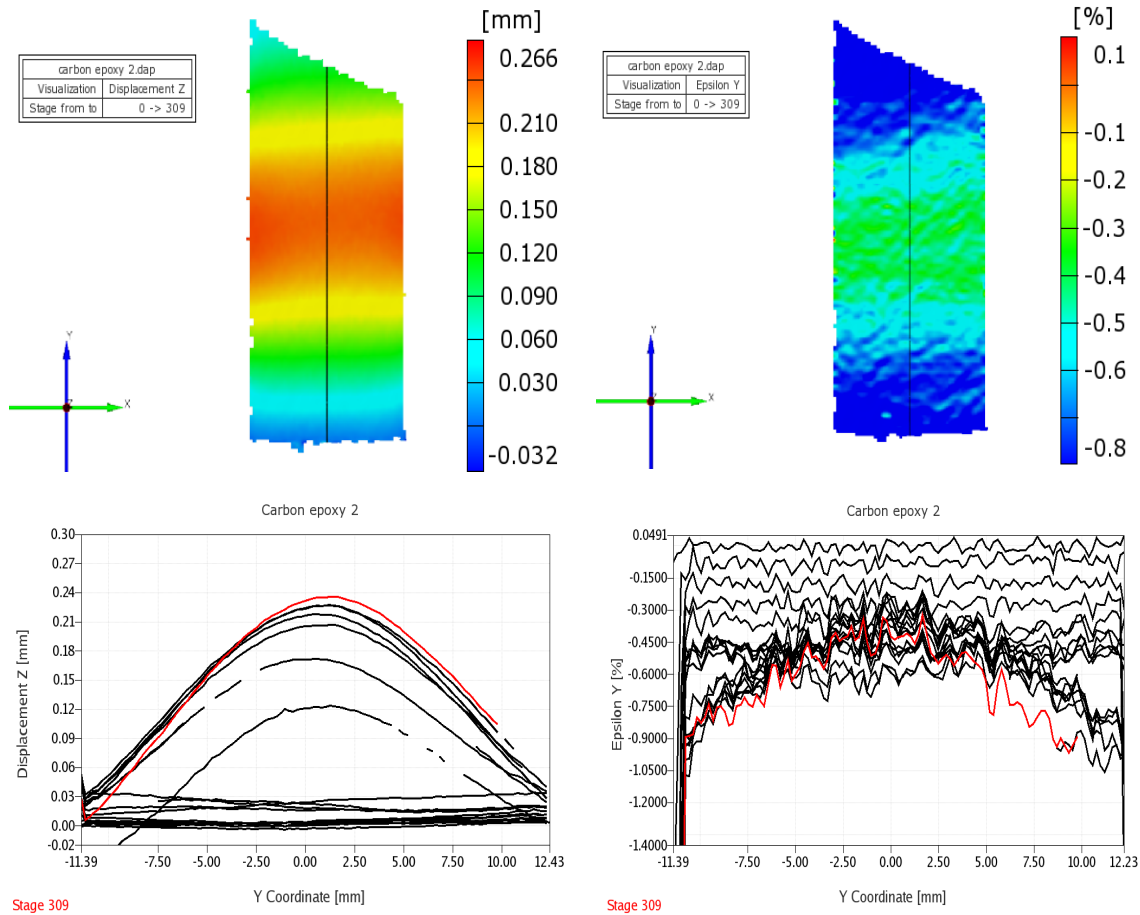


Figure 32. DIC measurements for the carbon composite sample 2, failure recorded after 4 seconds at  $20 \text{ W/cm}^2$ . Out of plane displacement (upper left), axial strain (upper right), with lower left and right showing lineouts taken along the black line in the photos above.

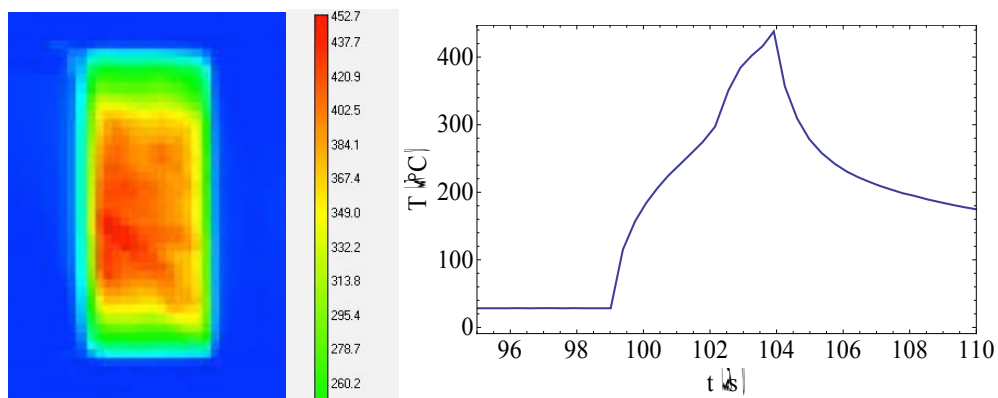


Figure 33. Infrared imaging camera measurement of the sample temperature moments prior to failure. The graph on the right shows the measured temperature at the center of the shown image as a function of time.

A second measurement on carbon composite was made with laser irradiance of  $40 \text{ W/cm}^2$ . At this higher flux, failure occurred in about 2 seconds. The sequence of photos in Figure 34 clearly shows sample delamination followed by structural failure and finally ignition of flames. As failure occurred before the sample ignited, heat from burning was not a causal factor in the failure. The diode array remained on for about 4 seconds in total during this run. Figure 35 shows the sample after the test. Signs of the burned regions can be seen from the side.

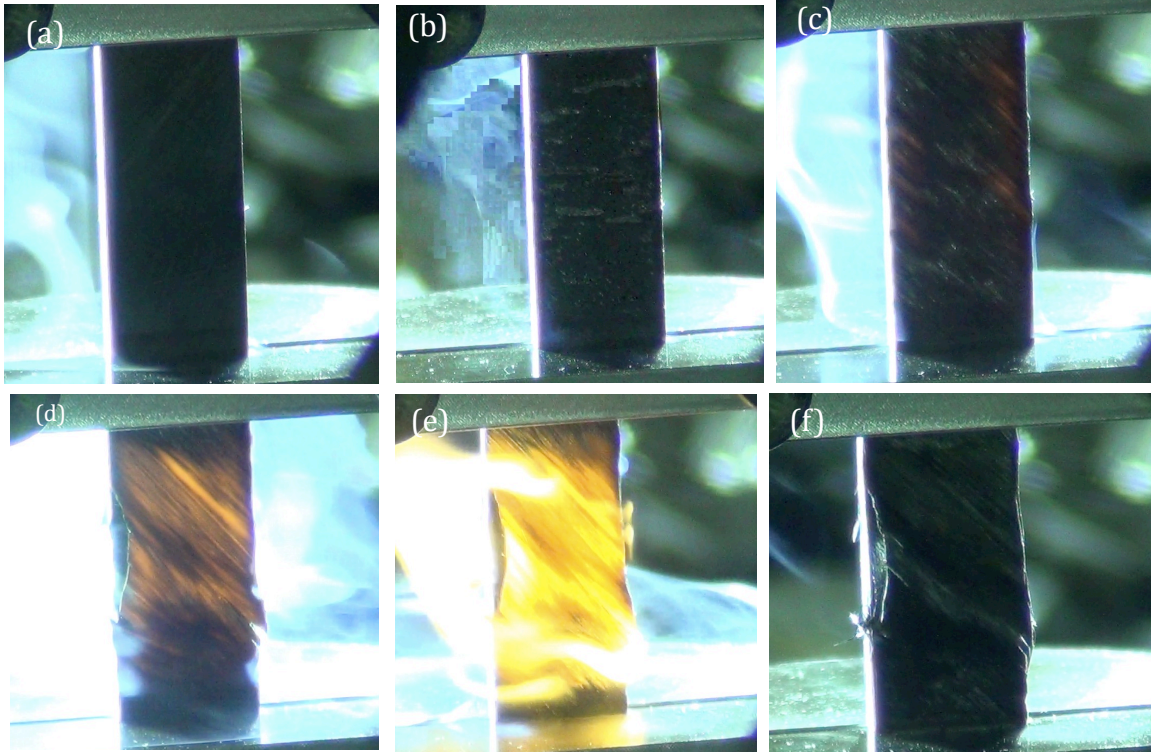


Figure 34. Carbon composite IM7/K3B of sample 3, load 276 MPa, irradiated at  $40 \text{ W/cm}^2$ . Time sequence is upper left to lower right: (a) laser on, smoke appears, (b) delamination begins, (c) surface starts to glow, (d) failure at 2 s, (e) sample burns after failure, (f) laser off – 4 s total irradiation.



**Figure 35. Post-irradiation photos of the carbon composite sample shown in Figure 34. Delamination is evident and burn marks are clearly visible.**

DIC measurements results, shown in Figure 36, indicate that the sample suffered more than 0.22-mm out-of-plane displacement toward the cameras moments before failure. The thermal image in Figure 37 indicates that the surface temperature exceeded 700°C before the sample burst into flames, which was the limit of the calibrated measurement range for the IR camera operational mode used during this test.

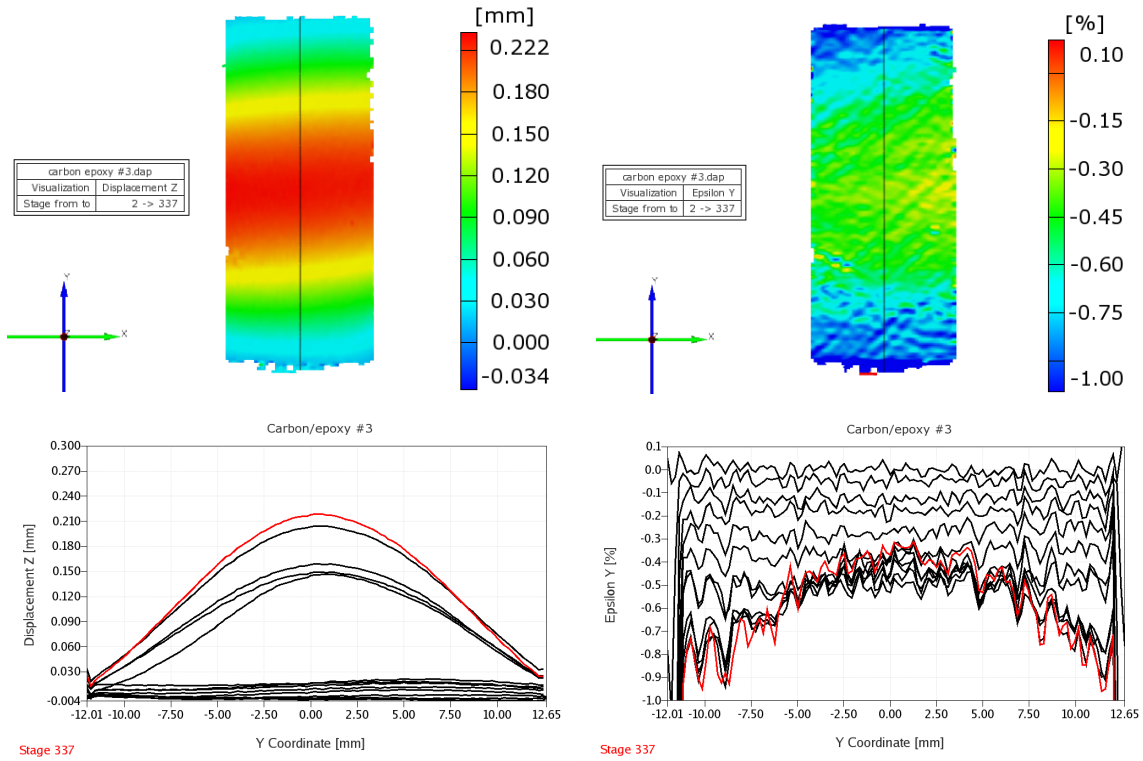


Figure 36. DIC measurements for the carbon composite sample 3,  $40W/cm^2$ , 1.5-s failure. Out of plane displacement (upper left), axial strain (upper right), with lower left and right showing lineouts taken along the black line in the photos above.

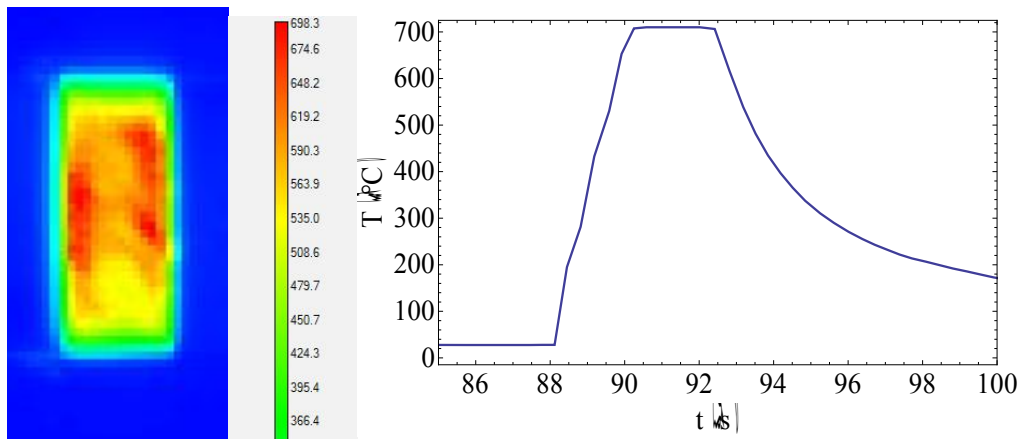


Figure 37. Thermal imaging camera data indicate that the surface temperature exceeded  $700^\circ C$  as the sample burst into flames, which was the limit of the calibration range for the IR camera measurement mode used on this test. The sample failed moments after this image was taken.

## FIBERGLASS COMPOSITE

Similar tests were conducted on the fiberglass composite samples composed of S-2 glass fibers in F155 epoxy resin matrix. These samples were more than 50% thicker than the carbon samples, but had lower baseline failure load strength. Test samples were preloaded to the 50% baseline load of 276 MPa. The fiberglass sample was irradiated at  $20 \text{ W/cm}^2$  and failure occurred at 5 seconds. Time-lapsed photos in Figure 38 show the break originated from the midsection of the sample. The epoxy can be seen to have softened and resolidified over the fractured surface. The sample failed without any evidence of pyrolysis or surface charring, as shown in Figure 39.

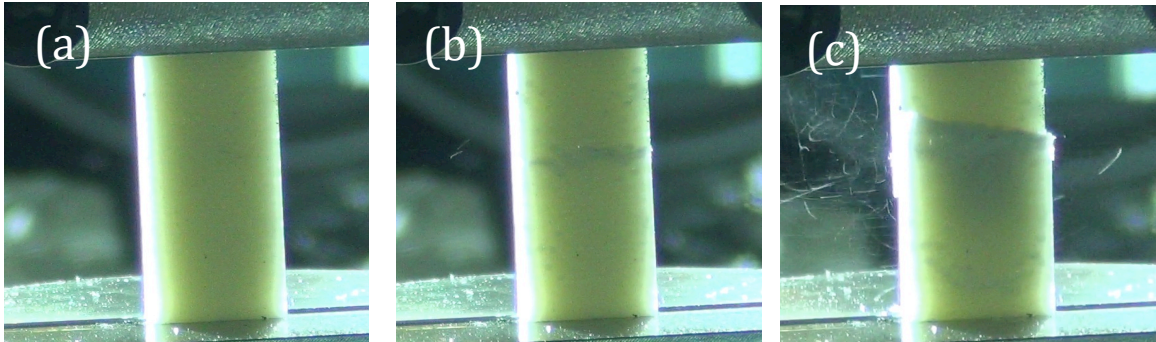


Figure 38. Fiberglass S-2/F155 sample 2, load 138 MPa, irradiated at  $20 \text{ W/cm}^2$ : (a) laser on, (b) internal damage visible, (c) failure at 5 s.

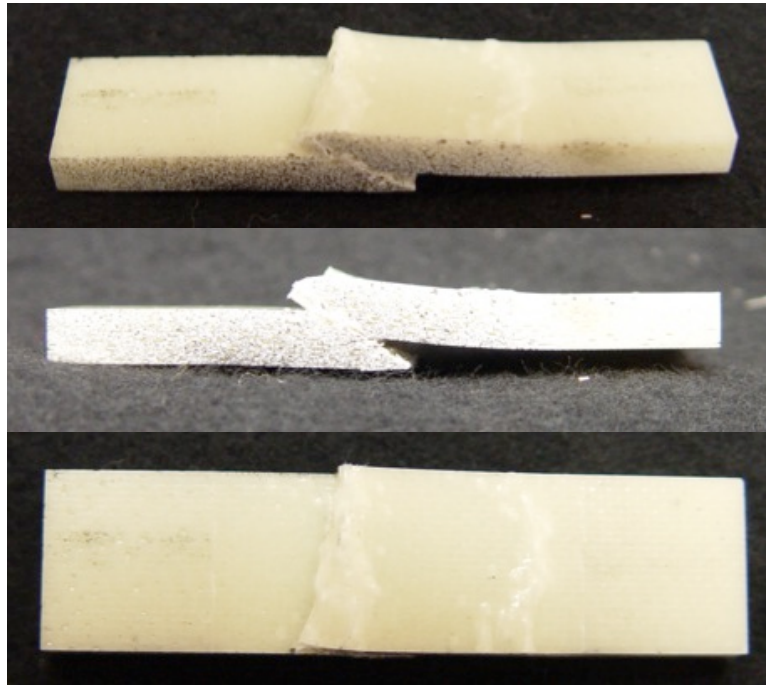


Figure 39. Post irradiation photos - fiberglass sample 2,  $20 \text{ W/cm}^2$ , failure after 5 seconds of heating.

DIC measurements, shown in Figure 40, indicate that the sample suffered more than 0.4 mm out-of-plane displacement toward the cameras moments before failure. Due to the semitransparency of fiberglass, heat is deposited directly in the sample interior rather than transported by

conduction. The axial strain is much more localized in this sample, probably due to this direct deposition of laser energy in the sample interior resulting in more localized heating. Figure 41 shows an infrared image of the sample moments prior to failure and temperature data on the sample.

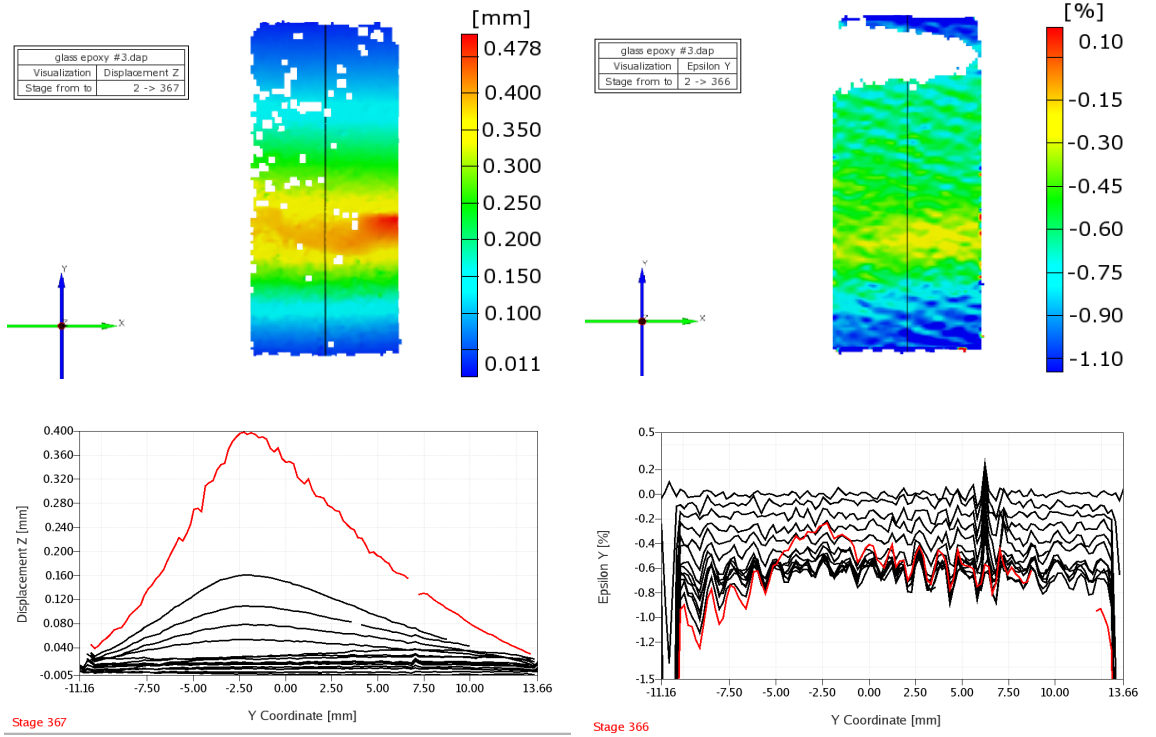


Figure 40. DIC measurements, fiberglass sample 2, 20 W/cm<sup>2</sup>, 5-s failure. Out of plane displacement (upper left), axial strain (upper right), with lower left and right showing lineouts taken along the black line in the photos above.

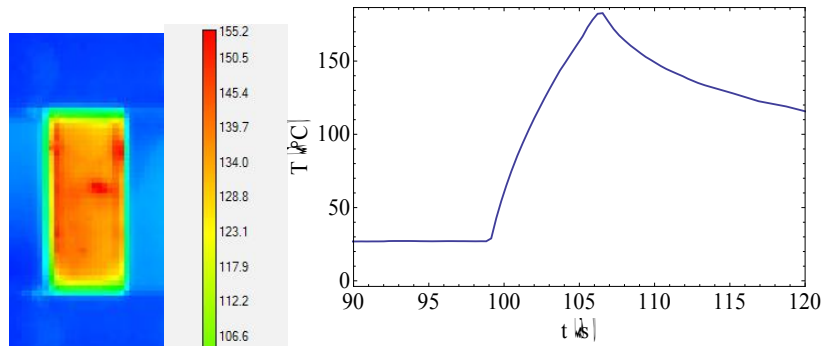


Figure 41. Infrared imaging camera measurement of the sample temperature moments prior to failure. The graph on the right shows the measured temperature at the center of the shown image as a function of time.

Similar results were found when the laser flux was reduced to 10 W/cm<sup>2</sup>. Lower intensity allows for more uniform heating inside the sample and reduces surface effects. Under this intensity, the sample failed after 7 seconds with fairly similar failure morphology, as shown in Figure 42.

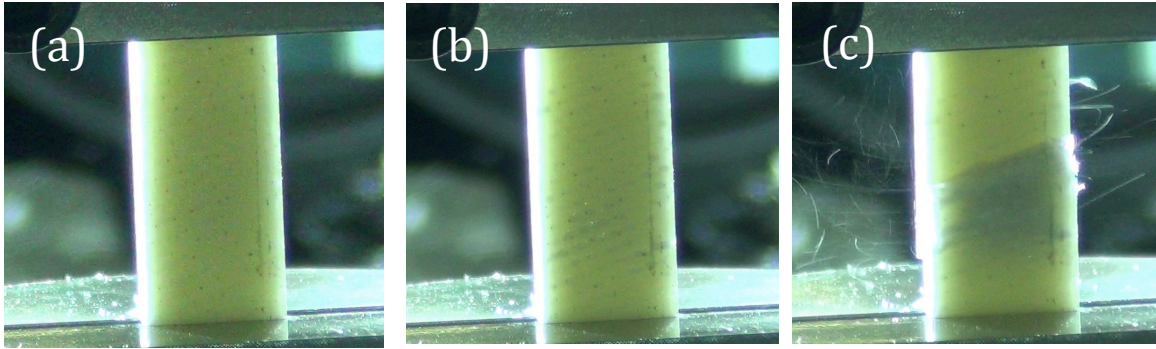


Figure 42. Fiberglass S-2/F155 sample 3, load 138 MPa, irradiated at 10 W/cm<sup>2</sup>: (a) laser on, (b) visible surface changes, (c) failure at 7 s. Small spots can be seen all over the front surface prior to failure.

DIC measurements, Figure 43, show more than 0.26 mm out-of-plane local displacement toward the cameras at failure. Thermal imaging data and temperature data are shown in Figure 44. Similarly, Figure 45 shows that the sample failed without any evidence of pyrolysis or surface charring.

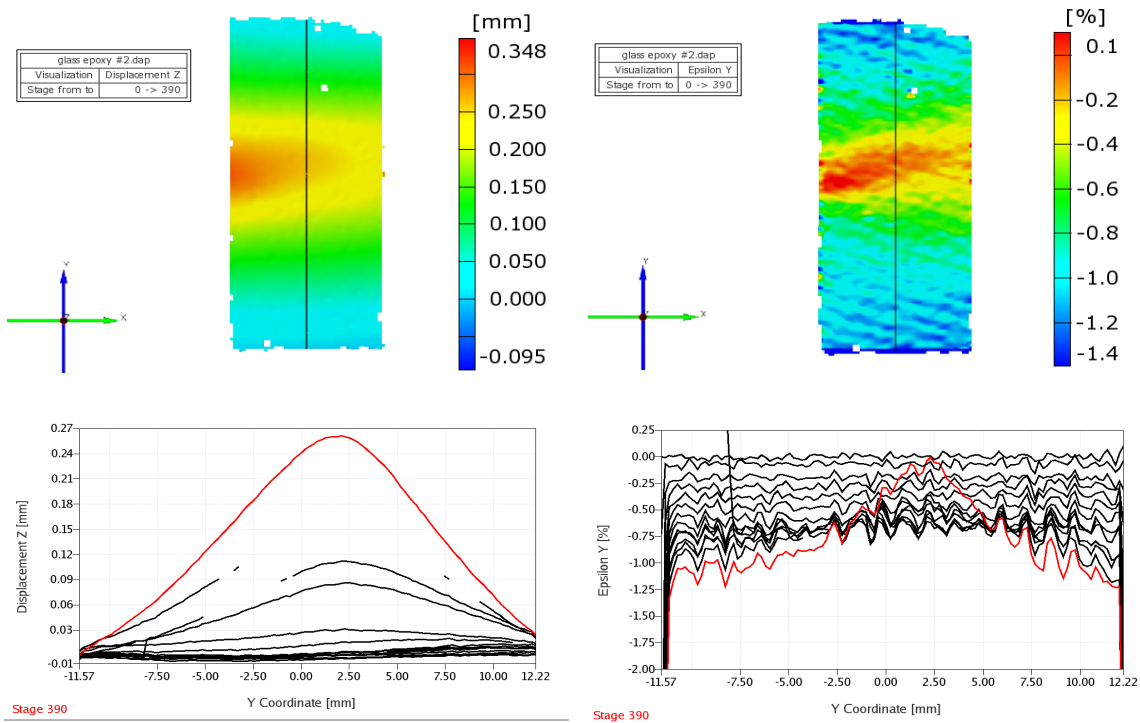


Figure 43. DIC data, fiberglass sample 3, 10 W/cm<sup>2</sup>, 7-s test run. Out-of-plane displacement (upper left), axial strain (upper right), with lower left and right showing lineouts taken along the black line in the photos above.

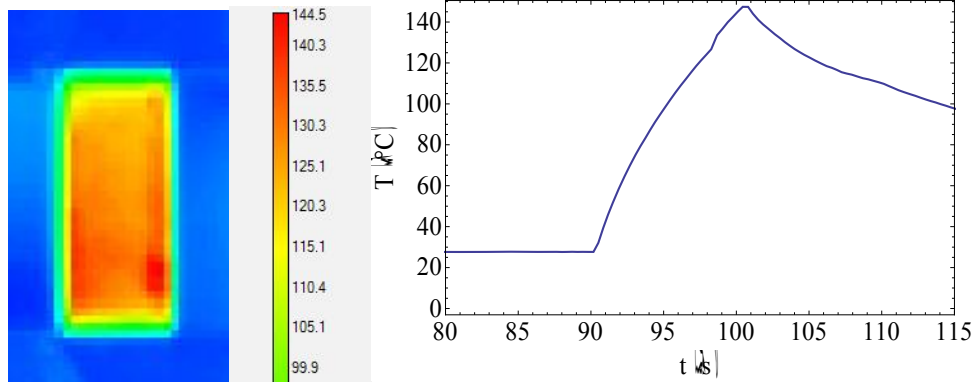


Figure 44. Infrared imaging camera measurement of the sample temperature moments prior to failure. The graph on the right shows the measured temperature at the center of the shown image as a function of time.

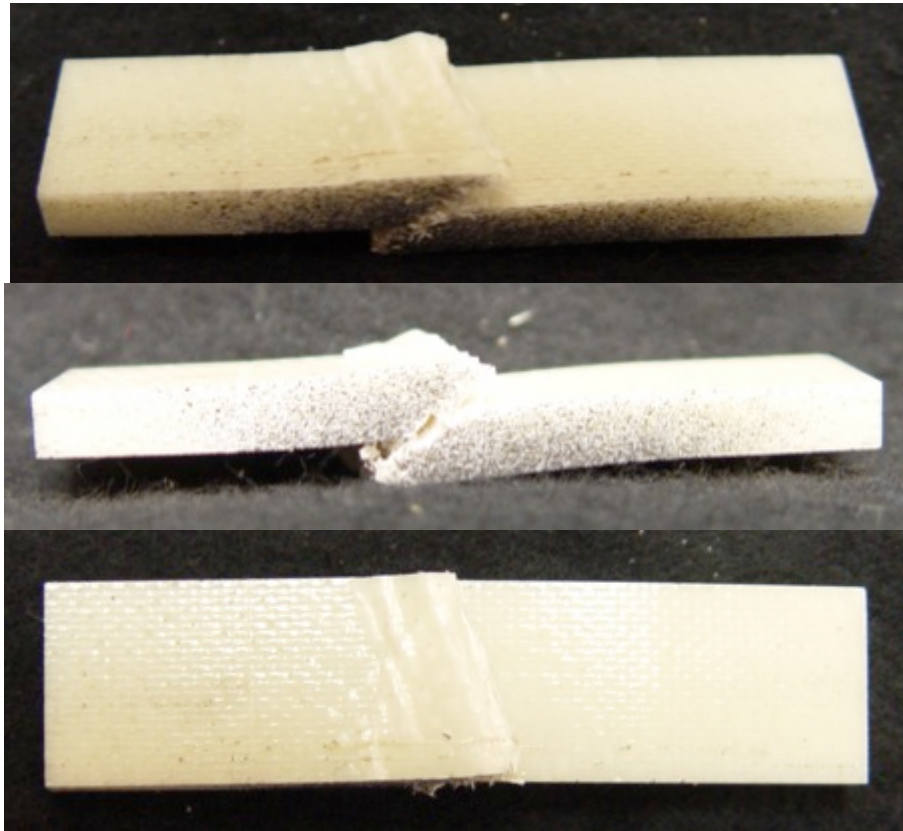


Figure 45. Post irradiation photos - fiberglass sample 3, failure after 7 seconds at  $10 \text{ W/cm}^2$ .

## CONCLUSION

The principal result of this Feasibility Study was the discovery that volume heating of fiber reinforced composite materials, either by direct in-depth absorption of laser energy, as in fiberglass material, or by rapid conduction of surface-deposited energy, as in carbon composites, can induce failure of aerospace structural composite materials under compressive load within a few seconds of irradiation by a near-IR laser at intensities less than 100 W/cm<sup>2</sup>. This value is one to three orders of magnitude lower than that required to produce lethal effect by target penetration or material removal. Composite material failure by any mechanism at such low flux has not been previously reported and has significant laser lethality and vulnerability implications.

A detailed ray-trace model was developed for composite materials to calculate absorptivity, reflectivity, and localized field enhancement due to scattering and interference. This ray-trace model works well to describe carbon composites where the fibers strongly absorb the near-IR laser radiation. For fiberglass composites, where the radiation penetrates much deeper, microscopic ray-trace calculations are still valid but more time-consuming, and thus a macroscopic two-flux model, which utilizes parameters obtained from the ray-trace code, was developed. This approach to study light propagation and energy deposition in composite materials can be extended to other translucent materials as well as paints, and would be an integral part of a predictive thermo-mechanical description of material behavior under the effects of high-power laser radiation.

Finally, a method to accurately calibrate IR thermal cameras was developed and demonstrated effective for both metals, where thermal radiation is far from a blackbody, and for composites, where thermal radiation is close to a blackbody, but calibration may be sensitive to internal temperature gradients. The ability to provide accurate IR camera calibration greatly simplifies laser lethality studies by enabling remote temperature measurement of laser-irradiated materials and components.

## ACKNOWLEDGEMENTS

We gratefully acknowledge Mike King for providing composite material samples and technical advice, and Gina Bonanno and Gil Gallegos for administrative support. Completion of this Feasibility Study within allocated budget and schedule was made possible by use of experimental equipment and facilities established under LDRD FY2012 Project 12-ERD-050.

## REFERENCES

- Borghesi, A., and Guizzetti, G., *Handbook of Optical Constants of Solids II* (E. D. Palik, ed.), Academic Press 1981.
- Carslaw, H., and Jaeger, J., *Conduction of heat in solids*, Oxford University Press 1959
- Chen, J.K., et al, "A Study of Laser/Composite Material Interactions," *Composites Science and Technology*, 54 (1995) 35-44.

Cozzens, R.F., and Lloyd, C.T., *High Energy Laser Interaction with Organic Matrix Composites – Part I*, 2007.

Feldman, M., *Effects of elevated temperature on physical aging of a high temperature thermoplastic resin and composite*, Master's Thesis in Engineering Mechanics, Old Dominion University, Norfolk, VA, 1996

FRED ray-tracing application distributed by Photon Engineering, LLC, Tucson, AZ.

Freeman, R. K., Rigby, F. A., and Morley, N., "Temperature-Dependent Reflectance of Plated Metals and Composite Materials Under Laser Irradiation", *J. Thermophys. and Heat Transfer* 14, 305-312 (2000).

Ishimaru, A., *Wave Propagation and Scattering in Random Media*, Academic Press, NY (1978).

LDRD 12-ERD-050 annual report, Lawrence Livermore National Laboratory (2012).

Landau, L., Lifshitz, E., *Electrodynamics of Continuous Media*, Pergamon Press (1960).

Landau, L., Lifshitz, E., *Elasticity Theory*, Pergamon Press (1960).

Laughlin, W.T., Popper, L.A., Goldey, C.L., and Hinrichsen, R.L., "Damage Assessment and Repair of Laser-Irradiated Helicopter Structures," Final Report prepared for Aviation Applied Technology Directorate, U.S. Army Aviation and Troop Command under Contract No. DAAJ02-94-C-0028, PSI-1219/TR-1507, October (1997).

Lubin, G., *Handbook of Fiberglass and Advanced Plastic Composites*, Polymer Technology Series, Society of Plastics Engineers (SPE), Van Nostrand Reinhold, Co., 1969

Mudgett, P., and Richards, L., "Multiple Scattering Calculations for Technology", *Appl. Opt.* 10, 1485, 1971.

Stonesifer, F.R., and Wissinger, G.W., Survivability of GFRP Materials to Continuous Wave and Repetitively Pulsed Laser Irradiation, NRL Memorandum Report 6582, Naval Research Laboratory, Washington, DC, November 30, (1989).

Thermophysical Properties of Composite Materials, TPRL, Inc., Report Number 2263, Nov. 1999

Walters, C., Seibert, D.B., Childers, L.B., Cain, A., Laser Beam Penetration of Generic Composite Wing Components, DEPS High Energy Laser Lethality Conference, Gaithersburg Md. April, 2012.

Wolfe, W. L., and Zissis, G. J., *The Infrared Handbook*, Infrared Information Analysis Center, 1985.

Zeldovich, Ya., and Raizer, Y., *Physics of Shock Waves and High Temperature Hydrodynamic Phenomena*, Academic Press, NY, 1967.